

Constraining the Interiors of Asteroids Through Close Encounters

Jack T. Dinsmore,^{1*} Julien de Wit²

¹*Department of Physics, Massachusetts Institute of Technology*

²*Department of Earth, Atmospheric, and Planetary Science, Massachusetts Institute of Technology*

Accepted XXX. Received YYY; in original form ZZZ

ABSTRACT

We investigate the degree to which asteroid interior density distributions can be extracted from rotational velocity data gathered during a close encounter. We derive the equations of motion for an rigid asteroid's orientation and angular velocity to arbitrary order and use them to generate synthetic rotational velocity data for a representative asteroid on a close Earth encounter. Using Markov Chain Monte Carlo fits, we re-extract the density moments of the asteroid in a wide range of scenarios to measure the degree to which best-fitting parameter precision is affected. Specifically, we use many injection-retrieval tests to study fit precision's dependence on the asteroid's moment of inertia, observational precision and cadence, orbital parameters, and initial spin pole direction as well as the quantity of near-pericentre data and the central body oblateness. Finally, we discuss the degeneracy between the density moments and the actual density distribution and propose three models to construct a representative density distribution from fit results.

Key words: minor planets, asteroids: general – methods: data analysis

1 INTRODUCTION

Over the past twenty years, the increase in quantity and quality of high-sensitivity, all-sky surveys has prompted the discovery of numerous asteroids. Such advances have been made via ground-based surveys such as the Catalina Sky Survey Larson et al. (1998), Pan-STARRS Kaiser et al. (2002), and the Lincoln Near-Earth Asteroid Research project (LINEAR) Stokes et al. (2000), as well as space-based instruments such as the Wide-field Infrared Survey Explorer (WISE) mission Wright et al. (2010). Many of these asteroids are relatively small, but some are kilometre-sized and a few are predicted to encounter Earth or other planets closely in the near future. Light curve analysis has been performed on many of these new asteroids to study their surface properties, but analyses that are sensitive to the interior structure of the asteroid are rarer.

Theoretical work has demonstrated that tidal torque alters the angular velocity of an asteroid during a gravitational encounter with another body, and that this tidal torque is sensitive to the interior density distribution of the asteroid Paul (1988); Scheeres et al. (2000); Ashenberg (2007); Boué & Laskar (2009); Hou et al. (2017). This two-body generalized system has been studied to different orders and with several different methods. The angular velocity changes in-

duced by tidal torque occur both in asteroid binaries Naidu & Margot (2015); Makarov et al. (2022), and during planetary encounters Richardson et al. (1998); Scheeres et al. (2004). Such asteroids need not be tidally disrupted for their rotation state to be perturbed by tidal torque. Some examples of rotational velocity altered during an encounter have recently been observed, including for the 2013 encounter of (367943) Duende with Earth Moskovitz et al. (2020); Benson et al. (2020), and have been predicted for the 2029 encounter of (99942) Apophis with Earth Scheeres et al. (2005); De-Martini et al. (2019). The upcoming encounter of Apophis is of particular interest and much attention has been devoted to accurate estimates of its orbital and physical properties Yu et al. (2014); Hirabayashi et al. (2021); Valvano et al. (2022); Lee et al. (2022), and in particular how its angular velocity will be affected by tidal torque Souchay et al. (2014, 2018). Altered rotational states altered by Solar tidal torque have been excluded for 1I/2017 U1 ‘Oumuamua Kwiecinski et al. (2018).

Such asteroid encounters have further been shown to reveal the physical properties of the encountering asteroid. Refs. Moskovitz et al. (2020); Benson et al. (2020) extract best-fitting dimensions for a triaxial ellipsoid model of Duende from light-curve data, and Refs. Descamps et al. (2020) and Berthier et al. (2020) extract bulk densities and rotational periods for asteroid binaries (3905) Doppler and (617) Patroclus respectively.

* E-mail: jtdinsmo@mit.edu

More encounter candidates are likely to be discovered in the future — for Earth or other planets — potentially by the James Webb Space Telescope (JWST) or Large-aperture Synoptic Survey Telescope (LSST), and general methods for assessing whether an asteroid’s encounter properties are conducive to the extraction of physical asteroid characteristics from light-curve data is necessary. However, such general encounters are not very well studied, since much of previous research has focused on specific encounters.

Furthermore, asteroid properties which appear in the beyond-leading-order terms of tidal torque have not yet been extracted, and more research is needed to study in what cases these effects are observable.

In this paper, we address these two topics by deriving a new equation of motion for an asteroid encounter system in section 2. This equation is simple and exact to arbitrary order, given assumptions reasonable for a planetary encounter (and many binary asteroid systems). It is also fast in that it allows volume integrals over the asteroid to be pre-computed. We use this equation of motion to simulate a generic asteroid encounter of Earth, and extract physical characteristics of the asteroid (specifically, density moments) from synthetic data via a Markov Chain Monte Carlo (MCMC) fit, described in section 3.1. We measure the uncertainties in the posterior distribution of density moments as a function of various encounter parameters such as the observational uncertainty, cadence of observation, encounter orbital parameters, and more. We express which parameters most affect the precision of fit results in section 4. Finally, we propose methods to extract full density distributions with uncertainties from these density moments in section 5. We test the behaviour of these methods, highlight their strengths and weaknesses, and suggest ways in which they may be altered to suit the needs of the user.

2 METHODS

In this section, we describe our coordinates (section 2.1) for an encountering asteroid’s position and orientation, and we parametrize its density distribution via its “density moments” (section 2.2). Then we derive an arbitrary-order equation for tidal torque (section 2.3), write the equations of motion for the system (section 2.4), and describe a simulation used to integrate the equation of motion and produce synthetic data of angular velocity over time (section 2.5).

2.1 Coordinates

Throughout this paper, we assume that the asteroid under study is on a hyperbolic encounter with periape r_p and excess velocity v_∞ . We do not consider any third-body perturbations, and we assume that the body being encountered (the central body, e.g. a planet) is much more massive than the asteroid.

We make use of two frames of reference to model this system. One is the “inertial frame,” with axes denoted by $\hat{\mathbf{X}}, \hat{\mathbf{Y}}, \hat{\mathbf{Z}}$ and origin placed at the central body’s centre of mass and each axis aligned with an asteroid principal axis. $\hat{\mathbf{X}}$ points from the central body to the asteroid periape and $\hat{\mathbf{Z}}$ points parallel to the orbit angular momentum. We

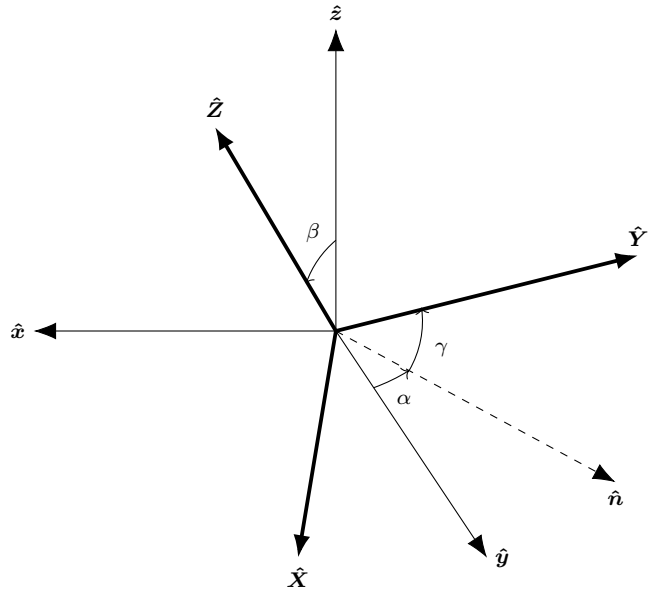


Figure 1. $z - y - z$ Euler angles used in this work to express the orientation of the asteroid. Orientation is expressed as a rotation from the body-fixed axes (lowercase) to the inertial axes (bold and uppercase). The origins are co-located for demonstration purposes.

will assume that the mass distribution of the central body is known in this inertial frame.

Our second frame is the “body-fixed” frame, denoted by $\hat{\mathbf{x}}, \hat{\mathbf{y}}, \hat{\mathbf{z}}$. This frame is fixed with respect to the asteroid’s principal axes and rotates with the asteroid, with its origin at the asteroid’s centre of mass. We will solve for the asteroid’s mass distribution with reference to the body-fixed frame. For definiteness, we define $\hat{\mathbf{z}}$ to be the principal axis with maximal MOI. In general, we use capital letters to denote vectors in the inertial frame and lowercase vectors to denote vectors in the body-fixed frame.

The difference between the origins of the body-fixed and inertial frames is the position of the asteroid. We represent the relative orientations by $z - y - z$ Euler angles α, β , and γ , such that a matrix M rotating from the body-fixed to the inertial frame ($M\mathbf{r} = \mathbf{R}$) is given by

$$M = R_z(\alpha)R_y(\beta)R_z(\gamma). \quad (1)$$

Here, $R_i(\theta)$ is a rotation around the unit vector i by θ (figure 1).

2.2 Parameters: density moments

In the next section, it will be shown that only certain parameters of the asteroid density distribution affect tidal torque called “density moments.” First, we define the unnormalized spherical harmonics $Y_{\ell m}(\theta, \phi) = P_{\ell m}(\cos \theta)e^{im\phi}$, where $P_{\ell m}$ are the associated Legendre Polynomials without the Condon-Shortley phase. The regular and irregular

spherical harmonics then defined as:

$$\begin{aligned} S_{\ell m}(\mathbf{r}) &= (-1)^m (\ell - m)! \frac{Y_{\ell m}(\hat{\mathbf{r}})}{r^{\ell+1}} \\ R_{\ell m}(\mathbf{r}) &= (-1)^m \frac{r^\ell}{(\ell + m)!} Y_{\ell m}(\hat{\mathbf{r}}). \end{aligned} \quad (2)$$

These spherical harmonics obey many useful identities summarized in Ref. van Gelderen (1998), which derives spherical harmonic identities useful for quantum mechanics.

We define the density moments of an asteroid as

$$K_{\ell m} = \frac{1}{\mu_A a_A^\ell} \int_A d^3 r \rho_A(\mathbf{r}) R_{\ell m}(\mathbf{r}). \quad (3)$$

Note that these are complex. Here, \mathcal{A} indicates the volume of the asteroid, μ_A is the mass of the asteroid, $\rho_A(\mathbf{r})$ is the density distribution, and a_A is a real length scale defined (for reasons covered later) as

$$a_A^2 = \frac{1}{\mu_A} \int_A d^3 r \rho_A(\mathbf{r}) r^2. \quad (4)$$

This length scale can be thought of as akin to the radius of the asteroid (although a spherical, uniform-density asteroid has radius $a_A \sqrt{5/3}$). Both equations 3 and 4 should be computed in the body-fixed axes.

Equations 3 and 4 can be extended to the central body:

$$\begin{aligned} J_{\ell m} &= \frac{1}{\mu_B a_B^\ell} \int_B d^3 r \rho_B(\mathbf{r}) R_{\ell m}(\mathbf{r}) \\ a_B^2 &= \frac{1}{\mu_B} \int_B d^3 r \rho_B(\mathbf{r}) r^2. \end{aligned} \quad (5)$$

which should be computed in the inertial axes.

Note that both $J_{\ell m}$ and $K_{\ell m}$ are unitless. We call them “moments” because the $R_{\ell m}(\mathbf{r})$ contains an r^ℓ dependence so that $K_{\ell m}$ is the ℓ th density moment of the asteroid. The gravitational potential field of the asteroid can be written entirely in terms of $K_{\ell m}$ and a_A , so we expect not to need any information about the density distribution of the asteroid beyond these parameters to compute tidal torque.

These moments share several key properties which we discuss before continuing. Firstly, for real mass density, properties of the spherical harmonics imply that $K_{\ell m} = (-1)^m K_{\ell, -m}^*$. Therefore, the set of $K_{\ell m}$ for $\ell < \ell_{\max}$ contains ℓ_{\max}^2 degrees of freedom. However, some of these degrees of freedom are redundant with the choice of coordinates as we discuss next.

By definition, $K_{00} = 1$. Furthermore, $K_{1m} = 0$ since the body-fixed frame is centred on the asteroid centre of mass. Further calculation reveals that the alignment of the body-fixed frame with the asteroid principal axes also forces $K_{21} = 0$ and $\Im K_{22} = 0$ and the same for $m < 0$. The only physical density moments for $\ell \leq 2$ are therefore K_{22} and K_{20} , which are related to the moment of inertia around each principal axis by

$$\begin{aligned} I_x &= \frac{2}{3} \mu_A a_A^2 (K_{20} - 6K_{22} + 1) \\ I_y &= \frac{2}{3} \mu_A a_A^2 (K_{20} + 6K_{22} + 1) \\ I_z &= \frac{2}{3} \mu_A a_A^2 (-2K_{20} + 1). \end{aligned} \quad (6)$$

Incidentally, the definition of a_A was chosen to satisfy equation 6.

ℓ	$\Re K_{\ell 3}$	$\Im K_{\ell 3}$	$\Re K_{\ell 2}$	$\Im K_{\ell 2}$	$\Re K_{\ell 1}$	$\Im K_{\ell 1}$	$K_{\ell 0}$
0							-
1					x	y	z
2			-	x,y	y,z	x,z	-
3	x,z	y,z	z	x,y,z	x	y	z

Table 1. Axes of mirror symmetry that imply zeroed density moments. For example, for mirror symmetries along $\hat{\mathbf{y}}$ or $\hat{\mathbf{z}}$, $\Im K_{32} = 0$. Mirror symmetry along $\hat{\mathbf{x}}$ means $\rho_A(x, y, z) = \rho_A(-x, y, z)$. Dashes indicate that none of the mirror symmetries zero the moment in question. Since $r^2 > 0$ for $r \neq 0$, no symmetries set $a_A = 0$ either.

The physical meaning of K_{22} and K_{20} can also be interpreted via a special case: if the asteroid is a uniform-density triaxial ellipsoid, the moments of inertia are simple to compute in terms of the semi-axis lengths and can be compared to those found in equation 6. This yields semi-axis lengths of

$$\begin{aligned} a &= \sqrt{\frac{5}{3}} a_A \sqrt{1 - 2K_{20} + 12K_{22}} \\ b &= \sqrt{\frac{5}{3}} a_A \sqrt{1 - 2K_{20} - 12K_{22}} \\ c &= \sqrt{\frac{5}{3}} a_A \sqrt{1 + 4K_{20}}. \end{aligned} \quad (7)$$

The physical meaning of the higher-order moments K_{3m} can be aided by assessing their symmetry properties. An asteroid that is mirror-symmetric along the $\hat{\mathbf{x}}$ axis (meaning $\rho_A(x, y, z) = \rho_A(-x, y, z)$) necessarily sets certain density moments to zero. Which density moments are zeroed by which mirror symmetries is outlined in table 1. Note that, while no mirror symmetries set K_{00} , K_{20} , or K_{22} equal to zero, mirror symmetries exist which zero all the other moments, including K_{3m} . $\Re K_{32}$, K_{31} , and K_{30} are the only K_{3m} components zeroed by only one axis. This will not affect our fit results for K_{3m} , but when we compute density moments for sample distributions, we find that most $K_{3m} = 0$.

Finally, the requirement that $\rho_A(\mathbf{r}) \geq 0$ everywhere restricts $K_{\ell m}$. In the case of K_{2m} , this fact and the constraint that I_z is larger than I_x or I_y requires K_{20} and K_{22} to fall in the triangle

$$-\frac{1}{4} \leq K_{20} \leq 0, \quad |K_{22}| \leq -\frac{K_{20}}{2}. \quad (8)$$

In practice, we also observe that $|K_{3m}| < 1$; often, $|K_{3m}| < 0.01$ even. For the rest of this paper, we therefore treat an uncertainty on $|K_{3m}|$ of 0.01 or less as a practical limit on observability, in that uncertainty greater than 0.01 means K_{3m} are effectively unknown. This is only a rough estimate, however.

2.3 Tidal torque

Derivations for the tidal torque experienced by a rigid body in the gravitational field of a larger mass have been computed by several previous studies Paul (1988); Hou et al. (2017); Boué & Laskar (2009); Ashenberg (2007), often in terms of the moment of inertia of the rigid body (or higher order moments of inertia), and to varying degrees of precision. A simple, first-order derivation is also easily computable in terms of the asteroid moment of inertia in the inertial frame.

Here, we present a novel derivation of the tidal torque to arbitrary orders in terms of the density moments of an asteroid defined in section 2.2. These density moments can be pre-computed and do not have to be re-evaluated every time-step.

Throughout this paper, we assume that the asteroid remains rigid throughout the encounter. We also assume no third-body perturbations from other Solar System objects. (Actually, third-body perturbing objects are allowed if they are closer to the central body's centre of mass than the asteroid perigee distance. Then, their density moments can be included in the density moments of the central body and this derivation can still be used.) For the sake of simplicity, we also assume that the density moments of the central body are known and do not evolve with time (i.e., the central body does not rotate).

The gravitational potential energy of the central body is, in its most general form,

$$V(\mathbf{R}') = -G \int_{\mathcal{B}} d^3 R \rho_{\mathcal{B}}(\mathbf{R}) \frac{1}{|\mathbf{R} - \mathbf{R}'|}. \quad (9)$$

where $\rho_{\mathcal{B}}$ is the density distribution of the central body and \mathcal{B} indicates the central body's volume. All vectors here are written in the inertial frame. Given $|\mathbf{R}| < |\mathbf{R}'|$, Ref. van Gelderen (1998) gives the identity

$$\frac{1}{|\mathbf{R} - \mathbf{R}'|} = \sum_{\ell, m} R_{\ell m}(\mathbf{R}) S_{\ell m}^*(\mathbf{R}'), \quad (10)$$

where the sum is shorthand for $\sum_{\ell, m} = \sum_{\ell=0}^{\infty} \sum_{m=-\ell}^{\ell}$. We are interested in translating the potential energy of equation 9 to the body-fixed frame. To do this, we let $\mathbf{R}' = \mathbf{D} + \mathbf{U}$, where \mathbf{D} is the location of the asteroid in the inertial frame. We further define $\mathbf{U} = M\mathbf{u}$, where \mathbf{u} is in the body-fixed frame and M is the rotation matrix given by the Euler angles α , β , and γ (see section 2.1). The translation from \mathbf{R}' to \mathbf{U} is then attained by the identity

$$S_{\ell m}(\mathbf{R}') = \sum_{\ell', m'} (-1)^{\ell'} R_{\ell' m'}^*(\mathbf{U}) S_{\ell + \ell', m + m'}(\mathbf{D}), \quad (11)$$

provided by Ref. van Gelderen (1998), and from \mathbf{U} to \mathbf{u} is given by

$$Y_{\ell m}(M\mathbf{u}) = \sum_{m'=-\ell}^{\ell} (-1)^{m+m'} \sqrt{\frac{(\ell-m')!(\ell+m)!}{(\ell+m')!(\ell-m)!}} \times \mathcal{D}_{mm'}^{\ell}(M)^* Y_{\ell m'}(\mathbf{u}). \quad (12)$$

Here, $\mathcal{D}_{mm'}^{\ell}(M)$ are the Wigner- D matrices, which are determined by the Euler angles α , β , and γ of M .

Equations 9 to 12 then provide formula for $V(\mathbf{u})$ expressed as a sum of integrals over \mathcal{B} of the central body density $\rho_{\mathcal{B}}(\mathbf{R})$ times $R_{\ell m}(\mathbf{R})$. These are expressed via equation 5 as $J_{\ell m}$.

The tidal torque experienced by the asteroid (in the body-fixed frame) is given by

$$\boldsymbol{\tau}(\mathbf{u}) = \int_{\mathcal{A}} d^3 u \rho_{\mathcal{A}}(\mathbf{u}) (\mathbf{u} \times (-\nabla_{\mathbf{u}} V(\mathbf{u}))) \quad (13)$$

where $\rho_{\mathcal{A}}$ is the density distribution of the asteroid and \mathcal{A} indicates the volume of the asteroid. Making use of one more

identity concerning the derivatives of spherical harmonics:

$$\begin{aligned} \mathbf{u} \times \nabla R_{\ell m}(\mathbf{u}) = & \frac{1}{2} \left[(i\hat{\mathbf{x}} - \hat{\mathbf{y}})(\ell - m + 1) R_{\ell, m-1}(\mathbf{u}) \right. \\ & + (i\hat{\mathbf{x}} + \hat{\mathbf{y}})(\ell + m + 1) R_{\ell, m+1}(\mathbf{u}) \\ & \left. + 2im\hat{\mathbf{z}} R_{\ell m}(\mathbf{u}) \right], \end{aligned} \quad (14)$$

tidal torque can now be expressed as a function only of $J_{\ell m}$, $K_{\ell m}$, $a_{\mathcal{A}}$, $a_{\mathcal{B}}$, and the asteroid orientation and position. Explicitly,

$$\begin{aligned} \boldsymbol{\tau} = & G \frac{\mu_{\mathcal{A}} \mu_{\mathcal{B}}}{2} \left[\sum_{\ell, m} a_{\mathcal{B}}^{\ell} J_{\ell m} \sum_{\ell', m'} a_{\mathcal{A}}^{\ell'} S_{\ell+\ell', m+m'}^*(\mathbf{D}) (-1)^{\ell'} \right. \\ & \times \sum_{m''=-\ell'}^{\ell'} \sqrt{\frac{(\ell' - m'')!(\ell' + m'')!}{(\ell' - m')!(\ell' + m')!}} \mathcal{D}_{m'm''}^{\ell'}(\alpha, \beta, \gamma)^* \\ & \times \left((i\hat{\mathbf{x}} - \hat{\mathbf{y}})(\ell' - m'' + 1) K_{\ell', m''-1} \right. \\ & \left. + (i\hat{\mathbf{x}} + \hat{\mathbf{y}})(\ell' + m'' + 1) K_{\ell', m''+1} + 2im''\hat{\mathbf{z}} K_{\ell'm''} \right) \right]. \end{aligned} \quad (15)$$

Some $K_{\ell m}$ terms are included in this equation with $|m| > \ell$; these should all be taken to be zero.

Equation 15 possesses a few explicit properties which we discuss before writing the asteroid equations of motion. Firstly, K_{00} does not appear, so that $\boldsymbol{\tau}$ is independent of asteroid mass. The mean density of the asteroid is therefore not constrained by tidal torque analysis. Secondly, torque is largest when D is small (as expected), with the leading order of $\boldsymbol{\tau}$ proportional to D^{-3} . Thirdly, each $J_{\ell m} K_{\ell'm'}$ term is multiplied by $(a_{\mathcal{B}}/D)^{\ell} (a_{\mathcal{A}}/D)^{\ell'}$, the latter of which especially is small in most cases. Equation 15 can therefore be computed approximately by removing terms of large ℓ and ℓ' . For our analysis, we remove $\ell' > 3$ and we usually keep only $\ell = 0$. Note that $\ell = 1$ contributes nothing since $J_{1m} = 0$.

Further insight can be gained by remarking the value of the first-order of $\boldsymbol{\tau}$ for particular Euler angle cases. Setting $\beta = 0$ produces diagonal Wigner- D matrices, and hence $\boldsymbol{\tau} \parallel \hat{\mathbf{z}}$ to first-order. Also, the component τ_z oscillates, so that for certain values of α and γ , $\boldsymbol{\tau} = 0$. This $\beta = 0$ condition is equivalent to $\hat{\mathbf{z}} \parallel \hat{\mathbf{Z}}$ (see figure 1).

For $\beta = \pi/2$, there are two interesting cases. One is for $\alpha = \phi$ (or $\alpha = \pi + \phi$), where ϕ is the angle between the asteroid and the perigee. In this case, $\boldsymbol{\tau} = 0$ to first-order. The second case is $\alpha = \phi \pm \pi/2$, when again $\boldsymbol{\tau} \parallel \hat{\mathbf{z}}$ and τ_z oscillates. At perigee ($\phi = 0$), these conditions are equivalent to $\hat{\mathbf{z}} \parallel \hat{\mathbf{X}}$ and $\hat{\mathbf{z}} \parallel \hat{\mathbf{Y}}$ respectively.

The $\boldsymbol{\tau} \parallel \hat{\mathbf{z}}$ cases are interesting because they do not induce tumbling. If velocity is $\boldsymbol{\omega} \parallel \hat{\mathbf{z}}$ (a non-tumbling state, since $\hat{\mathbf{z}}$ is a principal axis), then $\boldsymbol{\omega} \parallel \mathbf{L}$ and $\boldsymbol{\tau} = \dot{\mathbf{L}} \parallel \dot{\boldsymbol{\omega}}$ so that $\boldsymbol{\omega}$ remains parallel to $\hat{\mathbf{z}}$ and non-tumbling. These cases of torque are additionally significant because not as many terms contribute to τ_z as to τ_x and τ_y .

2.4 Equations of motion

The equations of motion of the asteroid position \mathbf{D} are given by Newton's law of gravitation:

$$\dot{\mathbf{V}} = -\frac{G\mu_B}{D^3} \mathbf{D} \quad \dot{\mathbf{D}} = \mathbf{V} \quad (16)$$

Rather than derive equations of motion for the Euler angles (which suffer from gimbal lock), we instead represent the orientation of the asteroid with a quaternion $\tilde{\mathbf{q}}$ which can be converted into Euler angles to compute $\mathcal{D}(\alpha, \beta, \gamma)$. This quaternion evolves as

$$\dot{\tilde{\mathbf{q}}} = \frac{1}{2}\tilde{\mathbf{q}}\tilde{\boldsymbol{\omega}}. \quad (17)$$

for angular velocity $\boldsymbol{\omega}$ given in the body-fixed frame. The equations of motion of $\boldsymbol{\omega}$ in turn are given by

$$\begin{aligned} I_x\dot{\omega}_1 - \omega_y\omega_z(I_y - I_z) &= \tau_x \\ I_y\dot{\omega}_2 - \omega_z\omega_x(I_z - I_x) &= \tau_y \\ I_z\dot{\omega}_3 - \omega_x\omega_y(I_x - I_y) &= \tau_z. \end{aligned} \quad (18)$$

Equations 15 to 18 form a set of non-linear, first-order coupled differential equations in which can be numerically integrated. They are expressed in terms of the constant physical parameters $\mu_{M/m}$, $a_{M/m}$, $J_{\ell m}$ and $K_{\ell m}$ given the density moment-moment of inertia relations given by equation 6.

Note that equation 18 is independent of a_A to first-order in $\boldsymbol{\tau}$, because $I_j \propto a_A^2$ for all j and $\boldsymbol{\tau} \propto a_A^2$. Therefore, scaling a_A merely scales the value of the sub-leading-order contributions to $\boldsymbol{\tau}$.

2.5 Simulation design

We built a custom simulation in C++ to produce angular velocity data (in the inertial frame, where it is observed from Earth) as a function of time. This simulation requires as initial data (1) the orbital parameters of the asteroid r_p (perigee distance) and v_∞ (hyperbolic excess velocity); (2) the cadence of angular velocity observation Δt ; (3) the central body moments $J_{\ell m}$, mass μ_B , and radius a_B ; (4) the initial asteroid angular velocity in the inertial frame Ω_0 ; (5) the asteroid "radius" a_A ; and (6) the asteroid's density moments $K_{\ell m}$ and initial Euler angle γ_0 . All parameters except (6) are assumed to be known to high accuracy. One can imagine that a_A is approximated by light-curve analysis, but if not, it is still necessary to fix a_A or else the values of $K_{\ell m}$ are degenerate with a_A .

We further assume that the asteroid is initially not tumbling. Thus, the rotational velocity is aligned with a principal axis (assumed to be $\hat{\mathbf{z}}$, which maximizes moment of inertia). This sets $\beta = 0$ and we can further choose $\alpha = 0$. Thus, only the Euler angle γ_0 is necessary to provide initial data for the simulation.

We begin our simulation at $D = 10r_p$, with velocity predicted by Kepler's laws given by the orbital parameters. Since the leading order of the equations of motion is $\ell' = 2, \ell = 0$, this corresponds roughly to a torque of 10^{-3} times the maximum torque at perigee. Unless otherwise indicated, the simulation is terminated at $D = 10r_p$ as well.

With the simulation inputs specified, the equations of motion were integrated via the Runge-Kutta fourth order

method, with a variable time step

$$dt = dt_{\min} + 10^{-3}(dt_{\max} - dt_{\min}) \left[\left(\frac{D}{r_p} \right)^3 - 1 \right]. \quad (19)$$

The parameters dt_{\max} and dt_{\min} (20 and 10 seconds respectively) were chosen such that the error was ~ 100 times the floating point error, and that neighbouring values of $K_{\ell m}$ yielded significantly different spin pole data compared to floating point error. The data used to choose this dt was obtained using the reference asteroid configuration, described in appendix A.

3 INJECTION-RETRIEVAL TESTS

In this section, we discuss how we used the simulation described in the previous section to generate synthetic data and extract density moment posterior distributions from the data.

3.1 Fit process

Given synthetic data, an Affine Invariant Markov Chain Monte Carlo (MCMC) Ensemble sampler was used to generate posterior distributions from flat priors. We use the Python implementation `emcee` Foreman-Mackey et al. (2013). Our parameters were γ_0 , K_{20} , K_{22} , and K_{3m} (10 in total), and were bounded by $|\gamma_0| < \pi/4$, and bounds on K_{2m} given in equation 8. Note that γ_0 is degenerate with $\gamma_0 + \pi/2$ since this is equivalent to re-labeling $\hat{\mathbf{y}}$ as $\hat{\mathbf{x}}$ and $\hat{\mathbf{x}}$ as $-\hat{\mathbf{y}}$. The other bounds were $|K_{3m}| < 1$.

The MCMC was determined to converge when the fractional change in autocorrelation time (computed every 100 iterations) was one percent, and the number of iterations computed so far was more than 100 times the autocorrelation time. The MCMC fit also was set to terminate if more than 10^5 iterations were run, but this only occurred for fits in which the data was too low quality to resolve the parameters. 10^4 iterations was often required, which generally consumed about 7 hours of computation time on a super computer running 16 threads on 8 cores.

Before the MCMC was run, local minima in the likelihood were found via the Nelder-Mead algorithm implemented in `scipy` Gao & Han (2012). It was found that only one local minimum existed, except when $K_{22} = 0$ in which case rotational symmetry caused multiple values of γ_0 to be degenerate. Walkers were initialized near this local minimum, distributed with probability distributed as a Gaussian approximation of the likelihood, as determined via the inverse Hessian of the likelihood at the minimum. Due to the high sensitivity of the angular velocity data to density moments, the minimization procedure sometimes failed to isolate the minimum likelihood. Therefore, a simpler simulation without the K_{3m} terms of equation 15 was first used to minimize likelihood as a function of γ_0 and K_{2m} , and then the full simulation was used to find K_{3m} , with γ_0 and K_{2m} fixed. This tiered minimization process motivates us to call γ_0 and K_{2m} the "first-order parameters" and K_{3m} the "second-order parameters".

We further subdivided the minimization process by first minimizing with respect to data truncated at the point after

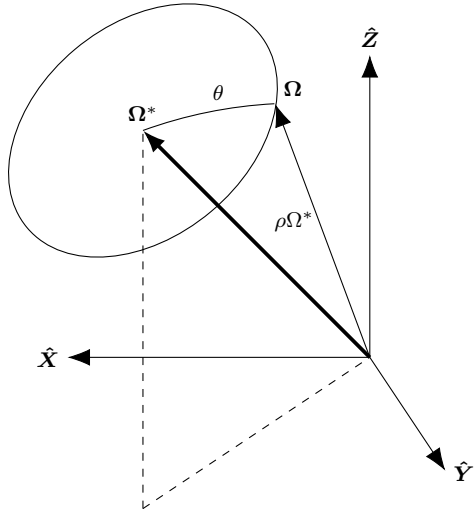


Figure 2. Diagram in the inertial frame of the uncertainty model used to define the probability that the true spin vector Ω^* should be observed as Ω . The parameter θ is drawn from a Gaussian with width σ_θ , and ρ is drawn from a log normal distribution with width σ_ρ .

perigee where $D = fr_p$ for some manually-set fraction f . In practice, $f = 2$ often led to success. The minimum was then further refined by minimizing based on the full data, with the previous minimum as the initial estimate.

3.2 Uncertainty model

We model uncertainty in each asteroid spin vector Ω in the as uncorrelated with other spin vectors, and we model uncertainty in the orientation and in the period as also uncorrelated. Consider a true spin vector Ω^* . For the sake of description, we work in coordinates in which $\Omega^* \parallel \hat{z}$. Then, expressing the observed spin vector Ω in spherical coordinates, we draw the polar angle from a normal distribution with standard deviation σ_θ centred on zero and the azimuthal angle from a uniform distribution. We also draw the ratio $\rho = \Omega/\Omega^*$ from a log-normal distribution centred on one, with width σ_ρ . We generally represent $\sigma_\theta > \sigma_\rho$ under the assumption that period is better constrained by light-curve data than spin pole. Explicitly, the probability density function (PDF) of ρ is

$$P(\rho) = \frac{1}{\rho\sqrt{2\pi\sigma_\rho^2}} \exp\left(-\frac{\ln^2 \rho}{2\sigma_\rho^2}\right). \quad (20)$$

See figure 2 for an illustration of the uncertainty model shown in the inertial frame.

The log likelihood resulting from this uncertainty model is (excluding additive constants)

$$\begin{aligned} \ln \mathcal{L} = -\frac{1}{2} \sum_{i=0} \left[\frac{\cos^{-1}(\Omega_i^* \cdot \Omega_i / (\Omega_i^* \cdot \Omega_i))^2}{\sigma_\theta^2} \right. \\ \left. + \frac{\ln(\Omega_i/\Omega_i^*)^2}{\sigma_\rho^2} + 2 \ln \frac{\Omega_i}{\Omega_i^*} \right]. \end{aligned} \quad (21)$$

where Ω_i is the i th spin vector in the data set.

In figure 3, we present example spin data generated via this simulation. A population of one thousand asteroids with

identical initial conditions except for γ_0 , K_{20} , and K_{22} were simulated on a close Earth encounter. The exact parameters used were the symmetric and asymmetric cases described in appendix A. Bands containing 68.3%, 95.5%, and 99.7% of the population's spin are shown, as is the spin of the reference asteroids in black.

To choose the initial values of γ_0 , K_{20} , and K_{22} , spin data for the reference asteroids of appendix A was first generated. Then γ_0 , K_{20} , and K_{22} were re-extracted via the fit described in section 3.1. The population's values for these parameters were posterior-distributed. However, the posterior distribution was widened by a factor of 1000 to make the band widths visible. Therefore, the scale of the bands in figure 3 have little meaning in an absolute sense, but they are meaningful when comparing two bands or two times in the same band.

The figure illustrates the sensitivity of spin data to asteroid density moments and γ_0 ; Before perigee, all asteroids had similar angular velocities, but after perigee the angular velocities of the population diverged. The oscillation periods observable during the torque-free precession phase of the spin data (about 5 hours after perigee) vary within the population, showing that they can be used to constrain K_{22} and K_{20} .

4 RESULTS

In this section, we assess the sensitivity of the posterior distributions for the first-order parameters (γ_0 , K_{20} , and K_{22}), and the second-order parameters (K_{3m}) to many possible close encounter configurations. Specifically, we test sensitivity to the encounter's orbital parameters, the degree of observational uncertainty, the asteroid's radius, the cadence of observation, the amount of data collected at perigee, the direction of the initial spin pole, the asteroid period, and the central body oblateness. These effects are presented roughly in order of how much they affect the parameter precision, from highest to lowest.

Parameter precision of 1σ is defined such that 68.27% of the posterior distribution lies within 1σ of the mean of the posterior distribution. 2σ is defined likewise for 95.45% of the posterior. The posteriors are usually roughly Gaussian, so that the upper and lower error bars are usually roughly equal and 1σ is approximately the standard deviation of the posterior.

In all cases, we use the configuration of the asymmetric reference asteroid (appendix A) unless otherwise stated. We further present a test of how precision depends on cadence, asteroid period, and the duration of the encounter in appendix B, and we compare precision for a Jupiter and an Earth encounter in appendix C.

4.1 Orbital elements

A Keplerian orbit is completely described by five parameters, but three describe the orbit's orientation with respect to the central body. The orbit can be rotated to the $\hat{X}\hat{Y}$ -plane, as mandated by our coordinate definitions, by changing the density moments of the central body. Since J_{00} is unchanged by this rotation and $J_{1m} = 0$, the orbit orienta-

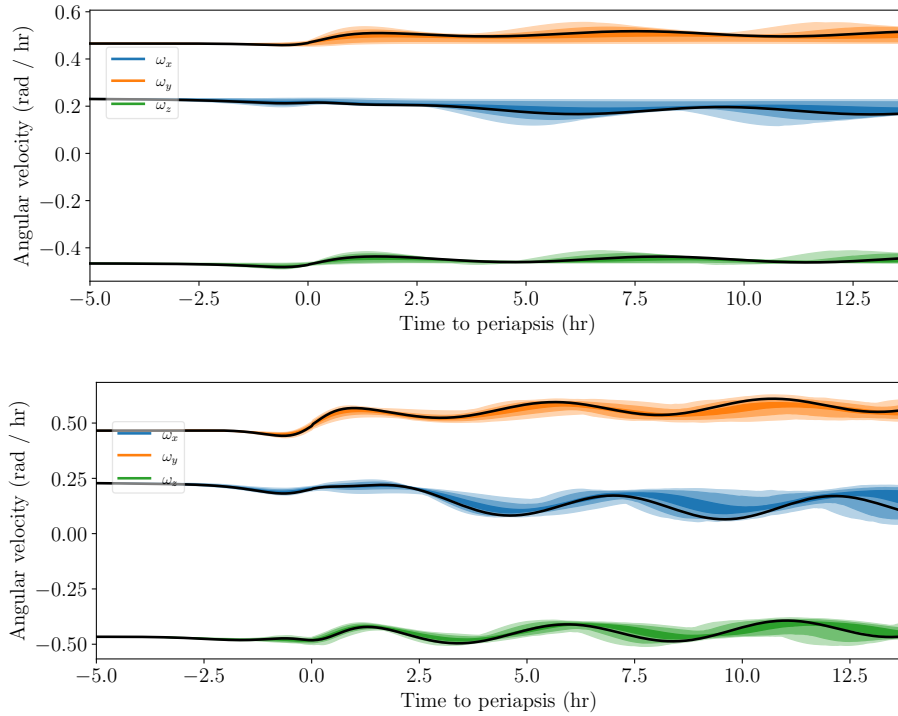


Figure 3. Angular velocity data simulated for the symmetric (above) and asymmetric (below) reference asteroids. The true angular velocity evolution is shown as a black line. Also plotted is the deviation of the data for posterior-PDF-distributed perturbations to the asteroid shape (bands). Bands contain 68.3%, 95.5%, and 99.7% of the 1000 simulations run.

tion is irrelevant until the J_{2m} terms of equation 15, and we do not investigate them here.

We parametrize the shape of the orbit by the perigee distance r_p and excess velocity v_∞ . Fits of the type described in section 3.1 were run for many values of r_p and v_∞ and the 1 and 2σ confidence intervals are displayed in figures 4 for v_∞ and 5 for r_p .

Figure 4 demonstrates that parameter precision does not depend strongly on excess velocity, aside from a slight trend especially in the higher order parameters for uncertainty to increase with v_∞ . This is likely due to the fact that larger v_∞ leads to a faster and flatter orbit with less time spent close to the planet, where tidal torque is strongest. There are also smaller-scale oscillations in the uncertainty, due to the orientation of the asteroid at perigee varying. The asteroid is always simulated to start at the same orientation, but increasing v_∞ decreases the time to perigee, so that the asteroid enters this region of high torque at different orientations depending on v_∞ . This effect explains why these small-scale oscillations have the same period for all parameters. Note that these oscillations are sometimes large enough to raise $\sigma > 0.01$, shown by the red vertical line.

Figure 5 shows much stronger dependence of parameter uncertainty on perigee distance, as expected by the factor of $(a_A/D)^{\ell'}$ present in equation 15 and mentioned in section 2.3. For $r_p \approx 6$ or 7 Earth radii, $\sigma(K_{30})$ reaches the reference 0.01 limit. At slightly higher r_p , K_{31} and K_{32} become similarly unresolved, and at $r_p \approx 20$ Earth radii, K_{33} , the last second-order component, becomes unresolved. Even before this, at $r_p \approx 10$ Earth radii, the most uncertain parameter K_{30} fills the prior distribution with uncertainty ranging from

Parameter	α
γ_0	2.05
K_{22}	5.47
K_{20}	5.47
$\Re K_{33}$	3.35
$\Im K_{33}$	3.37
$\Re K_{32}$	3.05
$\Im K_{32}$	3.27
$\Re K_{31}$	3.53
$\Im K_{31}$	4.02
K_{30}	5.75

Table 2. Power law slope values for the dependence of parameter uncertainty on perigee distance r_p . Slope is defined by $\sigma \propto r_p^\alpha$.

-1 to 1, visible by the sudden cut-off in uncertainty increase and the discontinuity of the σ curve there. The location of these limits will change if different encounter properties are used, but this is still an illustrative example.

Fitted to each of the curves in figure 5 are power law uncertainties $\sigma \propto r_p^\alpha$. These fits were performed via the method of least squares, and all data with $\sigma > 0.7$ was removed due to its sensitivity to the arbitrarily-chosen boundary of the prior. The values of α are shown in table 2. These slope values express how much each parameter is dependent on r_p . It is observed that γ_0 is least dependent on r_p , with $\sigma(\gamma_0) \sim r_p^2$. The other two first-order parameters are much more strongly dependent, with $\sigma \sim r_p^{5.5}$. The second-order parameters have milder slopes between 3 and 4 (except for K_{30}) which is fortunate from the perspective of making pre-

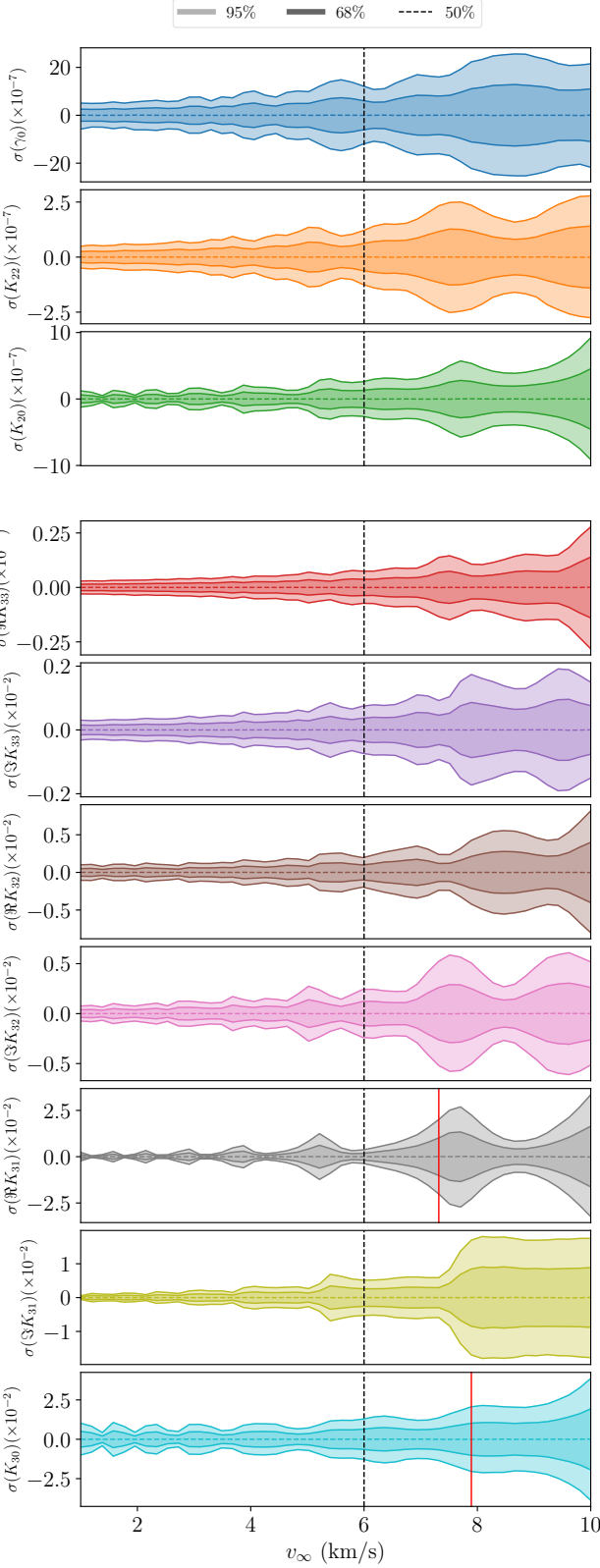


Figure 4. 1 and 2σ confidence intervals for the first-order parameter posteriors (*top*) and second-order parameters (*bottom*) as a function of orbital excess velocity v_∞ . The vertical dashed line indicates the reference asteroid value of 6 km s^{-1} . The red vertical lines indicate when $\sigma = 0.01$.

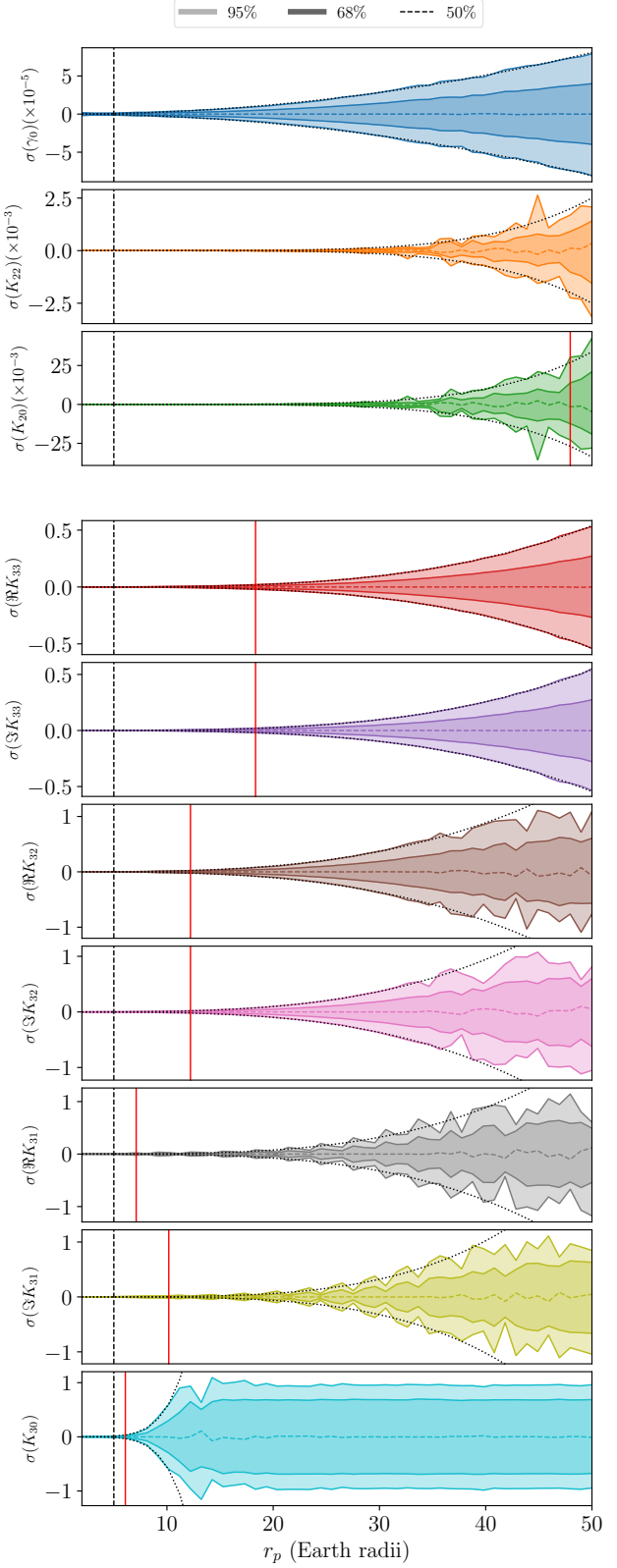


Figure 5. 1 and 2σ confidence intervals for the first-order parameter posteriors (*top*) and second-order parameters (*bottom*) as a function of perigee distance r_p . The vertical dashed line indicates the reference asteroid value of 5 Earth radii . The dotted curve indicates a power-law fit (see text). The red vertical lines indicate when $\sigma = 0.01$.

cise observations, since lower α renders larger values of r_p accessible to measuring K_{3m} .

The axes of figure 5 show that parameters with large m are more precisely determined than parameters with small m , as can be seen by comparing K_{22} to K_{20} and comparing K_{33} to other K_{3m} values. Large m moments correspond to moments that control higher frequency fluctuations in density at the asteroid equator. This pattern of large m corresponding to low uncertainty is a general trend and will be seen in the following sections as well.

The very strong dependence of σ on r_p makes this analysis only to extract second-order moments on close encounters. Fortunately, in the case of Earth, these encounters are also likely to have the best associated observational uncertainty when above the horizon due to their proximity. The first-order moments can still be extracted at much larger perigee distances in our model.

4.2 Observational Uncertainty

There are two parameters, σ_θ and σ_ρ , which govern the observational uncertainty of the data set (defined in section 3.2). Rather than explore the full space spanned by these two values, we measure how parameter uncertainties depend on the product of uncertainties $\sigma_\theta\sigma_\rho$ (with the radio fixed), and the ratio $\sigma_\rho/\sigma_\theta$ (with the product fixed).

We choose these metrics because we generally expect that the parameter uncertainty σ be proportional to the observational uncertainty, but whether the dependence is stronger on σ_θ or σ_ρ is not immediately clear. We get around this problem by varying σ_θ and σ_ρ together and fixing their ratio, and measuring the posterior uncertainty σ , with σ/σ_θ shown in figure 6. Indeed, we find that $\sigma \propto \sigma_\theta$ almost exactly, and since $\sigma_\rho/\sigma_\theta$ is fixed, we also have $\sigma \propto \sigma_\rho$. For large $\sigma_\theta\sigma_\rho$, the proportionality fails, but this is because $\sigma(K_{30}) \approx 1$ which fills the prior. Uncertainty cannot increase beyond this value.

We also investigate the dependence of posterior uncertainty on $\sigma_\rho/\sigma_\theta$ with $\sigma_\theta\sigma_\rho$ fixed in figure 7. If we simply had $\sigma \propto \sigma_\theta\sigma_\rho$, then σ would have no dependence on $\sigma_\rho/\sigma_\theta$. Any deviation from constant σ shown in the figure therefore reveals some additional dependence in the model on one of the observational uncertainties.

Indeed, figure 7 shows increased uncertainty when $\sigma_\rho/\sigma_\theta$ is large, so that σ depends more on σ_ρ than on σ_θ . We summarize this pattern by stating that, if the observer had to choose between better precision on the period or on the spin pole of the data, they should choose period. This is fortunate for observers since, **JTD: I want to say that precision on the period is better constrained by light curve analysis, but I do not know enough about light curve analysis to be sure.**

Another conclusion that can be drawn from figure 7 is that $\sigma(\sigma_\rho/\sigma_\theta)$ is proportional for all $K_{\ell m}$. The proportionality constant shows the same dependence on ℓ and m mentioned previously. The proportionality is broken near $\sigma \approx \pm 1$, where σ fills the prior.

The location of the $\sigma > 0.01$ limit demonstrates the great influence of observational precision on fit uncertainty; increasing $\sigma_\theta\sigma_\rho$ or $\sigma_\rho/\sigma_\theta$ by even a small amount raises $\sigma(K_{3m}) > 0.01$ in most cases.

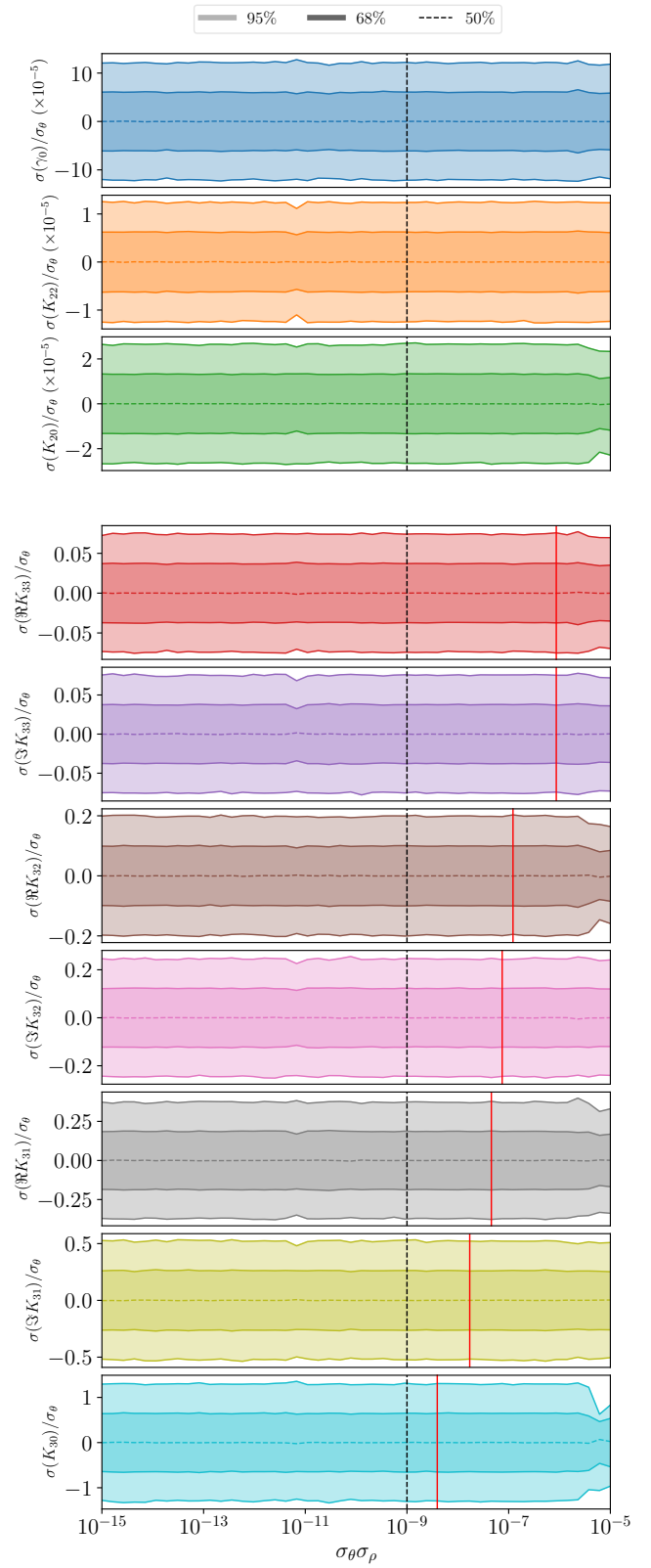


Figure 6. 1 and 2σ confidence intervals divided by σ_θ for the first-order parameter posteriors (*top*) and second-order parameters (*bottom*) as a function of observational uncertainty product $\sigma_\theta\sigma_\rho$. The vertical dashed line indicates the reference asteroid value of 10^{-9} . The red vertical lines indicate when $\sigma = 0.01$.

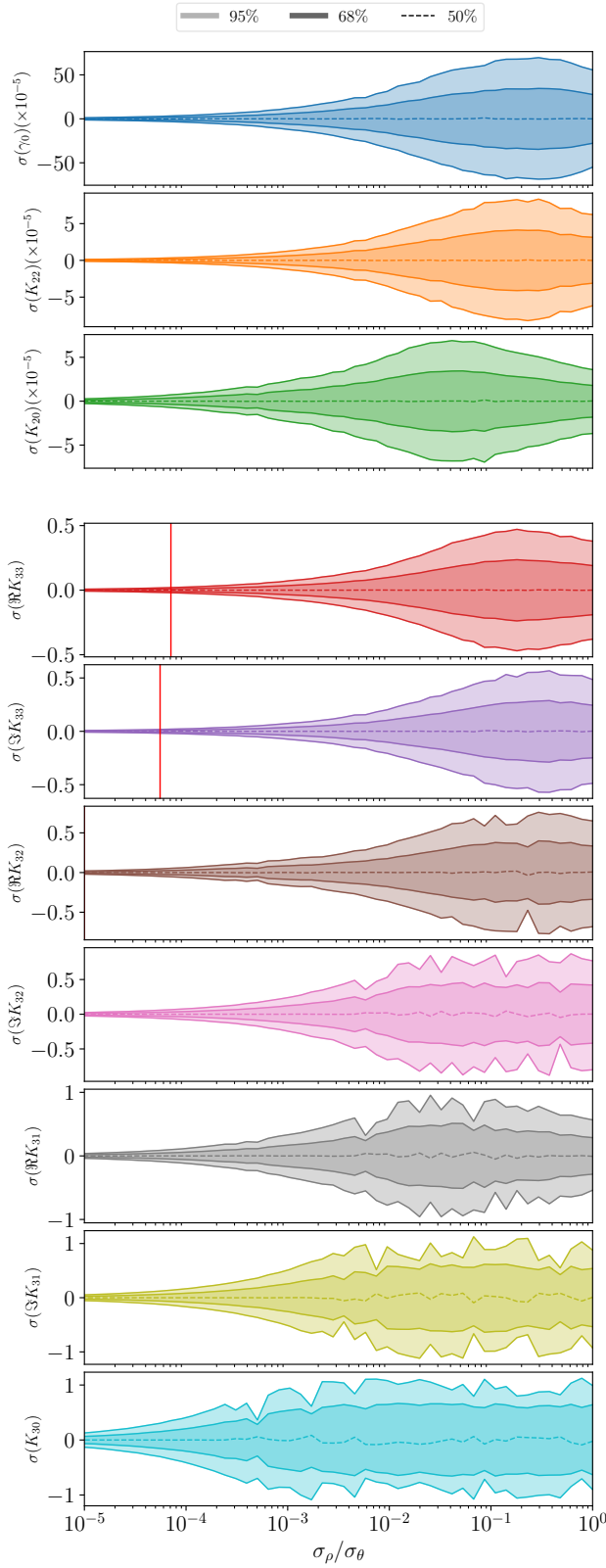


Figure 7. 1 and 2σ confidence intervals for the first-order parameter posteriors (top) and second-order parameters (bottom) as a function of observational uncertainty ratios $\sigma_\rho/\sigma_\theta$. The reference asteroid value is $\sigma_\rho/\sigma_\theta = 10^{-5}$. The red vertical lines indicate when $\sigma = 0.01$. (Lines are not shown for K_{3m} , $m < 3$ because they coincide with the vertical axis.)

4.3 Asteroid shape

The true values of $K_{\ell m}$, γ_0 , and $a_{\mathcal{A}}$ affect the uncertainties in extracted density moments σ . Here, we only investigate the sensitivity of σ to the first-order parameters and $a_{\mathcal{A}}$. The K_{2m} moments can therefore also be viewed as the axes of a uniform density triaxial ellipsoid (equation 7).

In figure 8, we show the 1σ confidence intervals as a function of K_{20} and K_{22} , or alternatively a/c and b/c . We use axis ratios rather than the values of a , b , and c to remove the $a_{\mathcal{A}}$ dependence of equation 7. The figure shows large uncertainty in γ_0 for $K_{22} = 0$, or $a/c = b/c$, because K_{20} is rotationally symmetric around $\hat{\mathbf{z}}$, and γ_0 is the initial orientation with respect to the $\hat{\mathbf{z}}$ axis. The data then have no physical dependence on γ_0 when $K_{22} = 0$. This induces degeneracy in the model which inflates uncertainties, not only in γ_0 but also the other components.

To remove the inflated uncertainty, one could assume a rotationally symmetric asteroid, remove γ_0 as a parameter, and run a fit. For a nearly rotationally symmetric asteroid however, a new parametrization is necessary which does not contain the ill-constrained γ_0 parameter. This task is beyond the scope of this paper, so we mostly consider asymmetric asteroids throughout.

Figure 8 also shows low uncertainty for highly asymmetric asteroids, where b/c and a/c are very different (i.e., when $|K_{22}|$ is large). Additionally, $\sigma(K_{20})$ and $\sigma(K_{22})$ decrease for large $|K_{20}|$, which corresponds to large axis ratios in the ellipsoid case.

Figure 9 displays the correlation between the first-order parameters for reference. They show that γ_0 and K_{22} are often correlated for asymmetric asteroids, while γ_0 and K_{20} are usually not. This is expected as K_{22} is dependent on the orientation of the asteroid and K_{20} is not. They also show that K_{22} and K_{20} are usually correlated, and that a/c and b/c are highly correlated. The latter is expected due to the $1/c$ dependence. As for the former, this correlation could likely be removed by an alternate parametrization, reducing uncertainties in the shape parameters.

Overall, the variation in the uncertainties on K_{20} and K_{22} (the first-order density moments) is present but largely smooth across their allowed parameter space, as is their correlation (except the large K_{22} corner). It therefore seems reasonable to use the asymmetric asteroid shape as a stand-in for an unknown's asteroid shape when simulating an encounter, as we do in this paper. The uncertainty then can be expected to differ across other shapes by a factor of about two or less, as long as the degenerate, symmetric asteroid regime is avoided.

On the other hand, the posterior uncertainty of K_{3m} is much more strongly dependent on asteroid “radius” $a_{\mathcal{A}}$. Figure 10 displays posterior uncertainty σ as a function of $a_{\mathcal{A}}$, defined in equation 4. The vertical axis is shown in log space, meaning that the average of the upper and lower error bars of σ is shown instead of showing both as is done in other figures.

As was mentioned in section 2.3, the K_{2m} parameters are insensitive to $a_{\mathcal{A}}$ since the $a_{\mathcal{A}}^2$ term in τ (equation 15) is canceled by the $a_{\mathcal{A}}^2$ in the moment of inertia (equation 6). The K_{3m} uncertainty is strongly dependent on $a_{\mathcal{A}}$ for the same reason that uncertainty is strongly dependent on r_p : the $(a_{\mathcal{A}}/D)^{\ell'}$ dependence of equation 15. At $a_{\mathcal{A}} \lesssim 700$

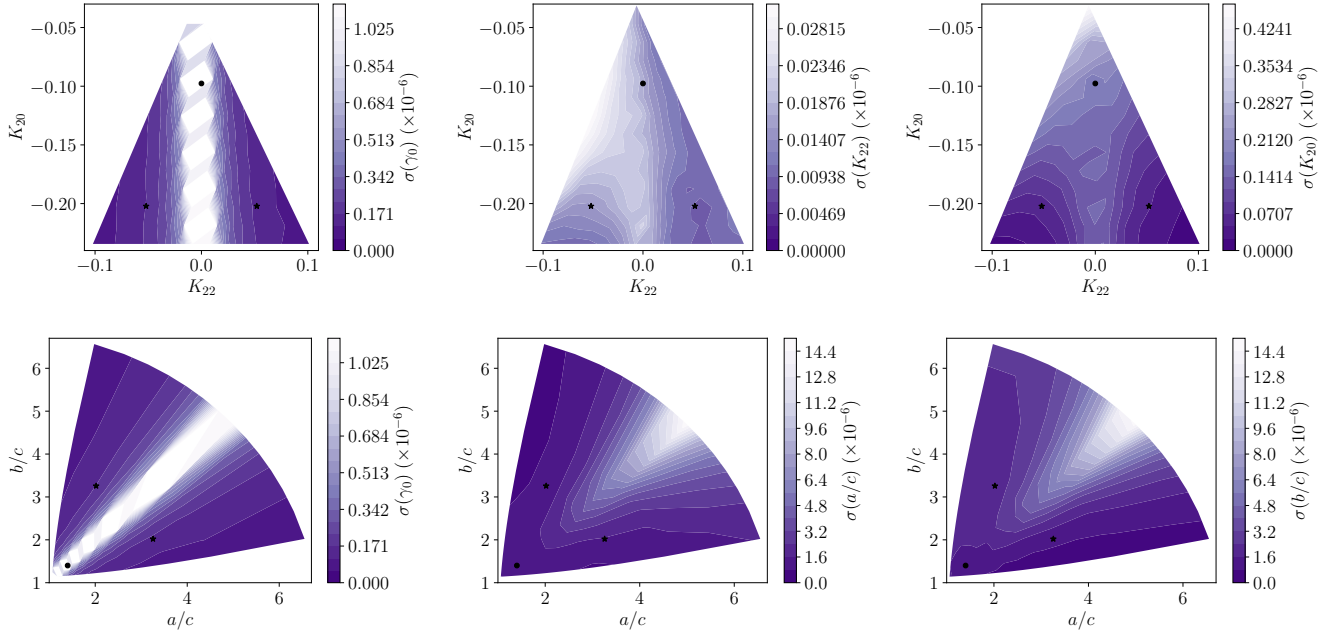


Figure 8. 1σ confidence interval for fit parameters γ_0 , K_{22} , and K_{20} (top row) and γ_0 , a/c , and b/c (bottom row). Also shown as black points are the reference asteroid shapes; the symmetric case is marked with a circle and the asymmetric with a star.

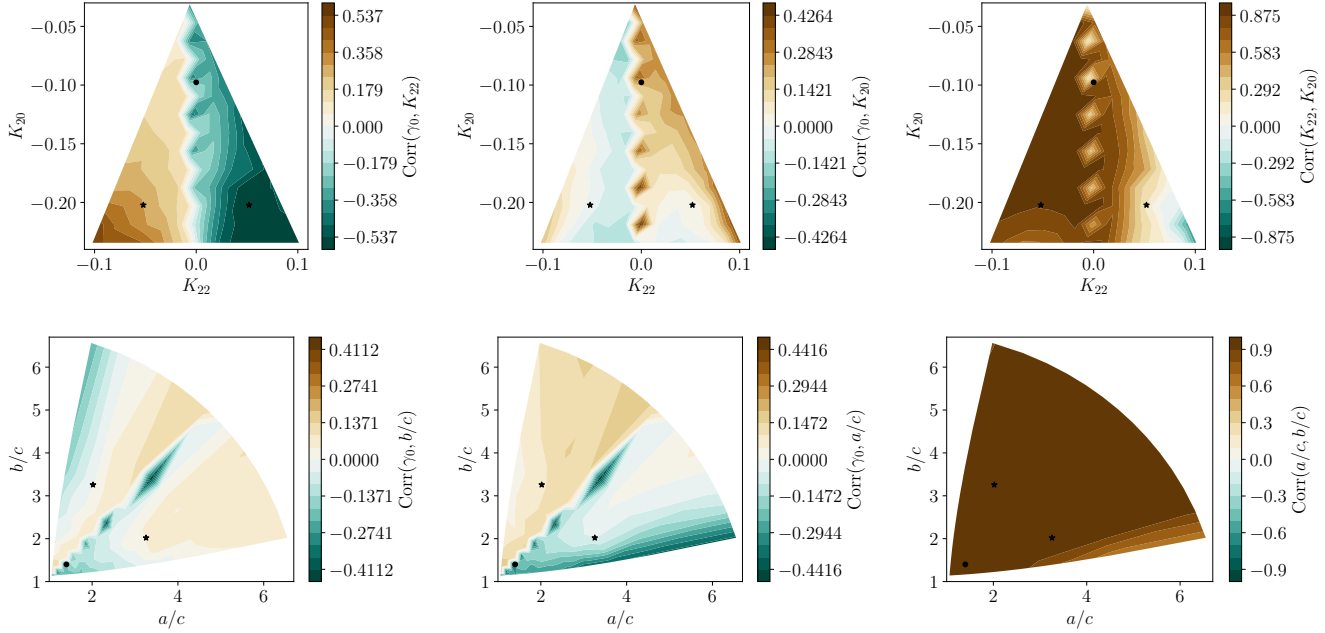


Figure 9. Correlations between parameter posteriors for fit parameters γ_0 , K_{22} , and K_{20} (top row) and γ_0 , a/c , and b/c (bottom row). Also shown as black points are the reference asteroid shapes; the symmetric case is marked with a circle and the asymmetric with a star.

parameters, K_{30} becomes unresolved. The other parameters become unresolved for $a_A \lesssim 300$ m, with the cut-off for K_{33} being less than 100 meters. This a_A cut-off is quite sharp; figure 10 shows steep decrease in $\sigma(a_A)$ for low a_A , with an approximate functional form of $\sigma(a_A) \sim e^{(a_A/C)^p}$ for a scaling constant C and some power $p < 1$. (In figure 10, the best fitting values are $p < 0.1$.) This sharpness indicates that the cut-off value of a_A is unlikely to change significantly if other

parameters of the flyby are altered in a way that slightly increases or decreases σ . It therefore appears that extracting precise K_{30} from asteroids with $a_A \lesssim 700$ m is very unlikely with this analysis, and for $a_A \lesssim 50$ m, all K_{3m} will likely be unresolved.

For uniform density asteroids, large a_A is equivalent to large asteroid radius, which was mentioned in section 2.2 and explicitly shown in equation 7. In non-uniform density

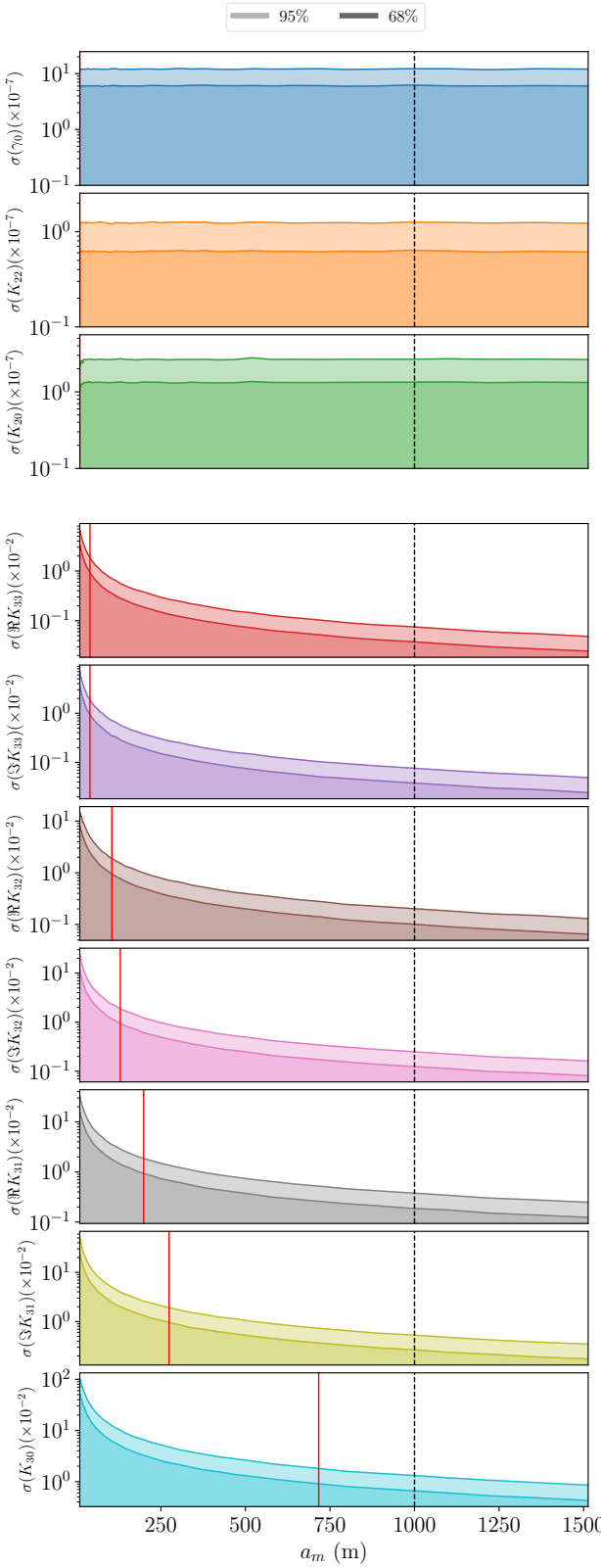


Figure 10. 1 and 2σ confidence intervals for the first-order parameter posteriors (top) and second-order parameters (bottom) as a function of asteroid “radius” $a_{\mathcal{A}}$. The reference cadence is 2 minutes. The red vertical lines indicate when $\sigma = 0.01$. The black dashed line indicates the reference value of $a_{\mathcal{A}} = 1000$ m.

asteroids, large $a_{\mathcal{A}}$ can also be achieved by distributing the mass of the asteroid near the surface, because the r^2 term in the integrand of the definition of $a_{\mathcal{A}}$ causes the density of regions distant from the asteroid centre of mass to dominate $a_{\mathcal{A}}$.

4.4 Cadence

The time between observations of asteroid angular velocity, or cadence, may vary depending on the observational schedule of the observing telescopes and the path of the asteroid through the sky. We measure how the posterior uncertainty σ varies with cadence ranging from two minutes to one hour in figure 11.

Figure 11 displays little dependence of uncertainty on cadence Δt for $\Delta t \lesssim 40$ min. We also see flaring of uncertainty for very large cadence, largely driven by the paucity of data points. However, uncertainty dramatically increases for many parameters at about $\Delta t = 30 - 40$ min, a time scale which is likely characteristic of the asteroid system. We name this rough cadence limit T_{cad} .

We expect T_{cad} to be a function of two dynamical time scales of the system: the rotational period of the asteroid P_{ω} and the time spent near perigee T_p . The latter can be estimated by

$$T_p \sim \frac{r_p}{v_{\infty}} \left[2 \frac{\mu_{\mathcal{B}}}{r_p v_{\infty}^2} + 1 \right]^{-\frac{1}{2}} \quad (22)$$

which is the ratio of the perigee radius to velocity at perigee. The exact choice of the formula of T_p not obvious, and alternatives to equation 22 are possible. For the simulated asteroid, $P_{\omega} = 9$ hr and $T_p = 42$ min by this definition.

We further study the effect of P_{ω} and T_p on T_{cad} in appendix B, and find that both affect T_{cad} by roughly the same amount.

Figure 11 shows that as long as $\Delta t < T_{\text{cad}}$ is achieved, the influence of cadence on σ is minimal (except for K_{30} where the $\sigma < 0.01$ limit is slightly exceeded). However, shorter cadence almost always leads to lower uncertainties.

4.5 Perigee gap

In certain circumstances, spin data might not be able to be captured for a close encounter at perigee. The asteroid might dip below the horizon, or it might pass too close to the sun to be observed. Generally, angular velocity data can be collected when the asteroid is distant from the central body, where torque is low. There, the angular velocity evolution is dominated by torque-free precession dictated by the moment of inertia components. That zero-torque data can still be used to fix K_{20} and K_{22} as in Moskovitz et al. (2020). However, K_{3m} are not extractable from precession data alone. We are therefore curious as to how our posterior uncertainties change due to lack of data during the encounter perigee.

To test this, we mask the perigee of the counter by removing a duration T of data centred on the perigee, where T ranges from 0 to 3 hours. To prevent lack of precision on $K_{\ell m}$ induced by lower amounts of data for high T , we always cut 3 hr – T from the data set, half from the beginning and half from the end, so that each data set produced for all T

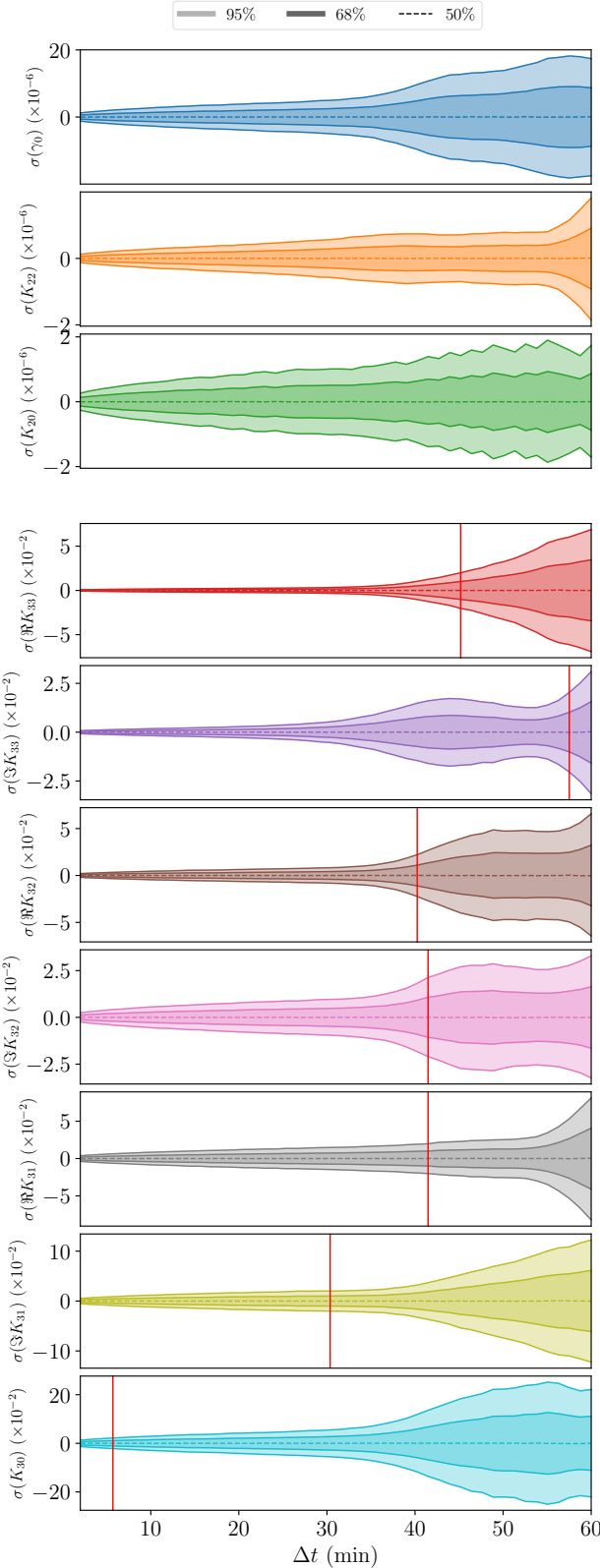


Figure 11. 1 and 2σ confidence intervals for the first-order parameter posteriors (top) and second-order parameters (bottom) as a function of observational cadence Δt . The reference cadence is 2 minutes. The red vertical lines indicate when $\sigma = 0.01$.

has the same length of data before and after the perigee. We then fit the same asteroid model to the cut data for all T and plot posterior uncertainties σ in figure 12.

Since torque is greatest at perigee, we expect that region of the data to contain the most information about $K_{\ell m}$, and therefore uncertainty should increase monotonically with T , which is seen in figure 12. We also see that the first-order parameters are not as sensitive to T as the second-order parameters, because K_{2m} are additionally constrained by torque-free precession after perigee.

Most parameters show dramatically increased uncertainty in the $T \sim 1 - 2$ hr range. On the other hand, none of the uncertainties increase noticeably for $T < 30$ min. Thirty minutes of dropped data is equivalent to fifteen dropped points for the simulated cadence of $\Delta t = 2$ minutes, showing that many data points can be dropped from the data set at perigee before the uncertainty starts to increase.

Qualitatively, 12 shows similar dependence of σ on T as 11 showed for σ on cadence Δt . They also both have cut-offs where uncertainty markedly increases, and both the T and Δt cut-offs have qualitatively similar shapes although they occur at different values of Δt and T . This suggests that the factors that govern uncertainty due to cadence (appendix B) also may govern sensitivity to lack of data at perigee in a similar way.

4.6 Initial spin pole

The tidal torque experienced by the asteroid is affected by the initial direction of asteroid spin Ω_0 both because spin sets the initial asteroid orientation up to γ_0 and because of the spin-dependence of the rotational equations of motion (equation 18).

In figure 13, we display 1σ uncertainties for all parameters as a function of the direction of Ω_0 , mapped onto the unit sphere in the inertial frame. Our samples for Ω_0 were laid out on a Fibonacci sphere to ensure they were roughly evenly spaced (marked in figure 14). To highlight common features across the parameters, we also display the average 1σ sensitivity in figure 14. The average is weighted such that the uncertainty map for each parameter contributes an equal amount (the weight of each map is set to one-tenth of the map's mean). This average map is presented in two different projections to allow data at \hat{Z} to be read.

Certain alignments of the body-fixed frame to the inertial frame lead to special conditions on torque, as discussed in section 2.3. For example, $z \parallel \hat{Z}$ and $z \parallel \hat{Y}$ at perigee lead to $\tau \parallel \hat{z}$ to first-order, and $\tau \parallel \hat{X}$ at perigee leads to $\tau = 0$ to first-order. We relate this to the initial direction of Ω_0 , via the approximation that τ is small until perigee. Then, since $\omega_0 \parallel \hat{z}$ in the body-fixed frame as an initial condition (section 2.5), we have that $\Omega_0 \parallel \hat{Y}$ and $\Omega_0 \parallel \hat{Z}$ both lead to $\tau \parallel \hat{z}$, and $\Omega_0 \parallel \hat{X}$ leads to $\tau = 0$.

Figure 14 shows area of increased uncertainty for $\Omega_0 \parallel \hat{Z}$ and $\Omega_0 \parallel \hat{Y}$, but not the \hat{X} case. This indicates that $\tau \parallel \hat{z}$ causes increased uncertainty. Physically, $\tau \parallel \hat{z}$ only changes an asteroid's rotational period and does not cause it to tumble, eliminating the ability to discern moment of inertia ratios from zero-torque precession after the encounter. Also, τ_z affected by fewer parameters than τ_x or τ_y . Both of these are reasons why $\tau \parallel \hat{z}$ might inhibit precise fits to spin data. If $\tau = 0$ to first-order, then second-order τ and

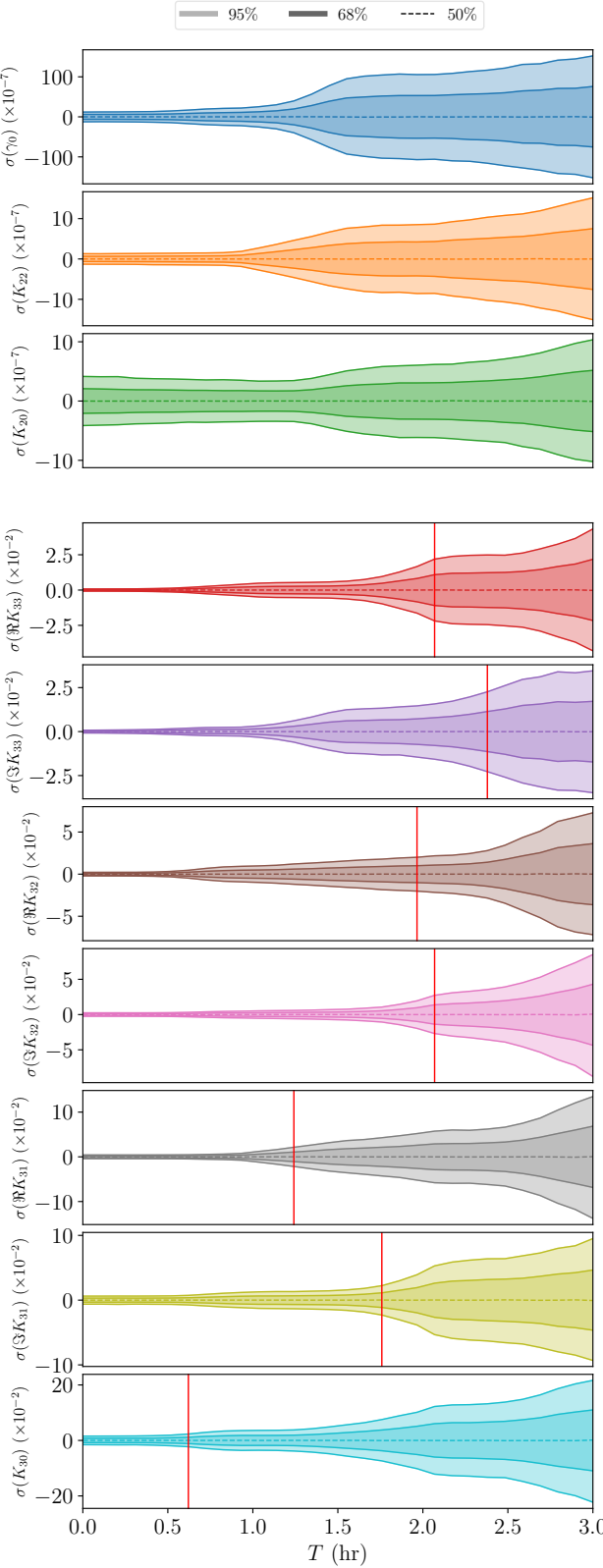


Figure 12. 1 and 2σ confidence intervals for the first-order parameter posteriors (top) and second-order parameters (bottom) as a function of a data gap of width T at perigee. The red vertical lines indicate when $\sigma = 0.01$.

non-perigee τ will dominate, which may increase precision to these usually non-dominant parameters and therefore not have the same increasing effect on σ .

It is important to note, however, that uncertainty does not vary by much more than a factor of two outside the imprecise regions of $\Omega_0 \parallel \hat{Z}$ and $\Omega_0 \parallel \hat{Y}$, though these regions are wide for some parameters. Within the imprecise regions, uncertainty can grow up to four times or more the uncertainty at other Ω_0 values, and can exceed the $\sigma = 0.01$ benchmark. The trends for are roughly consistent across parameters (figure 13), leading to clearly visible imprecise regions in the average σ (figure 14).

4.7 Rotational period

We also study the effect of the initial rotational period of the asteroid P_ω on posterior uncertainty σ . The dynamical time scales r_p/v_∞ and $\mu_B/(r_p v_\infty)$ have already been mentioned in the context of the cadence cut-off (section 4.4), and the ratio between them and P_ω in principal may affect σ . In figure 15, we show σ as a function of P_ω for a range of periods typical of NEOs.

Like figure 4, depicting the dependence of σ on v_∞ , figure 15 shows small-scale variation in uncertainty due to the fact that varying the initial period changes the value of γ at perigee, which affects uncertainty to a factor of about two. But a large-scale trend is also visible in many parameters. K_{20} and K_{22} show very large uncertainty for $P_\omega \lesssim 4$ hr because these fast-rotators tumble very little after perigee. This increases uncertainty on the K_{2m} parameters, which are constrained by tumbling.

We expect that quickly rotating asteroids would not tumble because, for small P_ω , the dynamical variables D , ω , α , and β vary much smaller than γ . Approximating each variable as constant over one full rotation of γ , we can integrate the first-order contribution of τ over $\gamma \in (0, 2\pi)$ and reveal that each rotation has zero average first-order torque. Since the first-order torque over each rotational period cancels out, there is no secular torque to force the asteroid to tumble. However, this effect does not apply to the second-order parameters, since the integral over the second-order term of τ does not vanish, as seen in the figure.

Another feature of figure 15 is that $K_{\ell 0}$ is more uncertain at low P_ω than the other parameters. This is most visible in the figure for K_{30} . The cause is likely that $K_{\ell 0}$ cannot contribute to τ_z as shown in equation 15. We already discussed that asteroids with small P_ω do not tumble, and since τ_x and τ_y are what induces tumbling, the most observable component of torque is therefore τ_z , which $K_{\ell 0}$ do not affect.

The most severe effect of period on σ is in the low-period regime ($P_\omega \lesssim 5$ hr), but in this case, the most strongly affected parameters are K_{2m} , which are generally known better than K_{3m} . The effect on the imprecise parameters K_{3m} is small, except for K_{30} . It therefore seems as though small-period asteroids are still candidates for observation, although high-period asteroids still have better uncertainty.

4.8 Central body oblateness

In all the above studies, we assumed a spherical planet ($J_{\ell m} = 0$ for $\ell \geq 1$). By assumption that $\mu_B \gg \mu_A$ (so

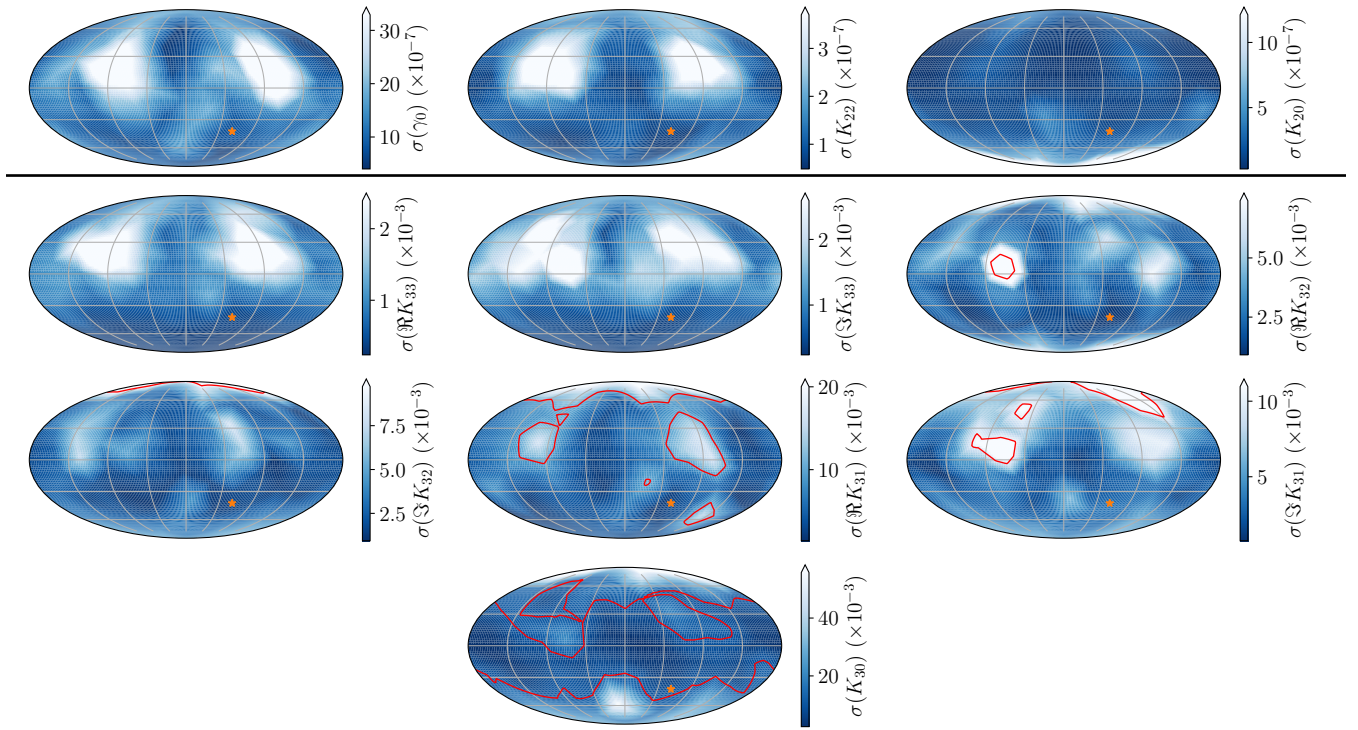


Figure 13. 1σ uncertainties for the first-order parameters (*top*) and second-order (*bottom*) as a function of the initial direction of spin in the inertial frame. All maps are made in the Mollweide projection. The orange star indicates the reference spin pole. The red contours enclose regions where $\sigma \geq 0.01$.

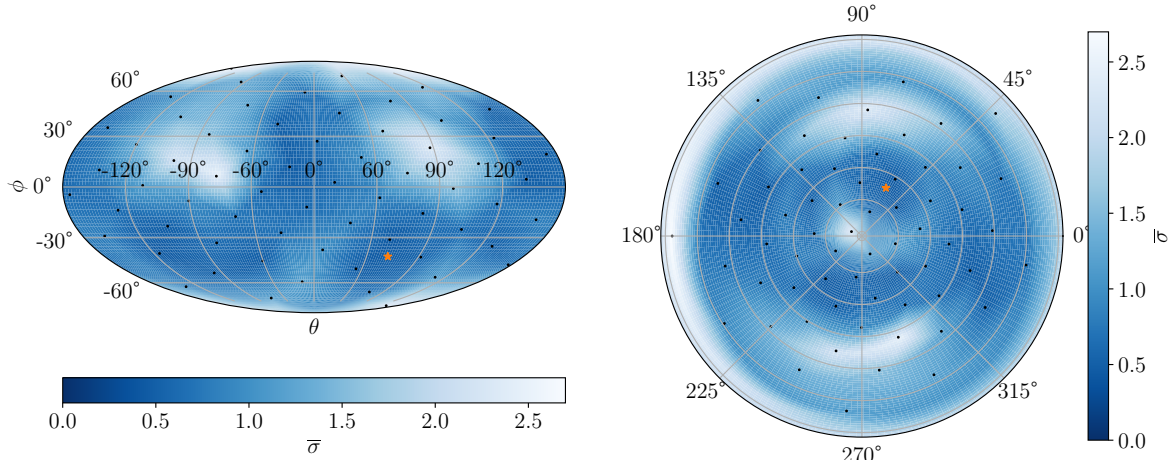


Figure 14. The weighted average of the uncertainties shown in figure 13, in Mollweide (*left*) and polar (*right*) projections in the inertial frame. See text for a description of how the average was computed. Black dots indicate the Fibonacci-sphere-distributed locations of sample spin poles, and the orange star indicates the reference spin pole. The polar projection is centred at the south pole, or $-\hat{\mathbf{Z}}$.

that the asteroid orbit's focus is the centre of mass of the central body), we have $J_{1m} = 0$. The effect of central body oblateness, then, is limited to the J_{2m} terms, and therefore damped by a factor of $(a_B/D)^2$. We expect these parameters to have little effect on the asteroid.

Here, we define oblateness as $\epsilon = (I_z - I_x)/(\mu_B R_M^2)$, where $I_{x,y,z}$ are the central body moments of inertia along

the principal axes, and $I_x = I_y$. R_M is the true radius of the body (not a_B from equation 5).

$J_{\ell m}$ is defined in equation 5 with respect to the asteroid orbit, not the principal axes of the central body. However, for an equatorial orbit, the central body principal axes coincide with the asteroid orbit frame and we may express ϵ simply in terms of $J_{\ell m}$ as $\epsilon = -2J_{20}$ and $J_{22} = 0$. (Some

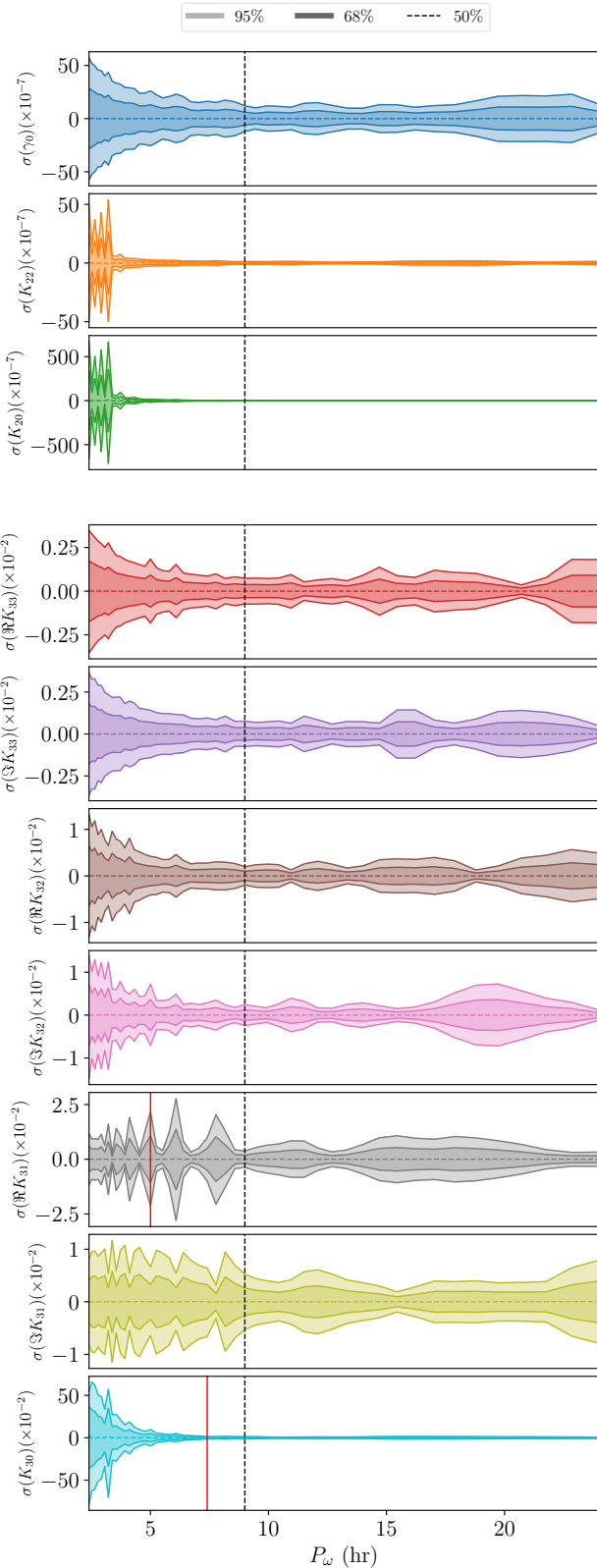


Figure 15. 1 and 2σ confidence intervals for the first-order parameter posteriors (*top*) and second-order parameters (*bottom*) as a function of initial rotational period P_ω . The reference value of 9 hr is shown as a vertical dotted line. The red vertical lines indicate when $\sigma = 0.01$.

sources such as Ref. [Pater & Lissauer \(2015\)](#) take $\epsilon = J_{20}$ as their definition of J_{20}). For simplicity, we use this equatorial orbit case. If the orbit is non-equatorial, the other J_{2m} terms will be non-zero. Since an oblate ellipsoid is mirror-symmetric around all three axes, table 1 indicates that J_{3m} are all zero. The next order of precision after this oblateness approximation is therefore J_{4m} , damped by an additional $(a_B/D)^2$ factor, and non-ellipsoid corrections to the central body shape.

Given this conversion between ϵ and J_{20} , we analyze posterior uncertainty σ of the first-order parameters as a function of ϵ across a reasonable range of central body oblatenesses based on those of Solar System planets [Pater & Lissauer \(2015\)](#). These uncertainties are shown in the top pane of figure 16, together with linear best-fitting curves for $\sigma(\epsilon)$.

The figure demonstrates a small dependence of σ on oblateness ϵ , but the effect is far from important compared to the other factors studied above. Most Solar System bodies do not reach the oblateness necessary to significantly increase precision on the first-order parameters. The best-fitting lines match the uncertainties well, and they have slope of $(\Delta\sigma/\sigma_{\epsilon=0})/\Delta\epsilon = -0.26$ for γ_0 , -0.94 for K_{22} , and -1.2 for K_{20} . The second-order parameters K_{3m} likely depend on oblateness similarly, but fitting these parameters is computationally more expensive and we do not study them here.

Note that if an encounter is executed around one of the non-Earth objects noted in figure 16, a_B and μ_B will change in addition to ϵ . These two parameters also affect the precision of the fit parameters (appendix C), so the figure does not show that encounters with other bodies have the same precision as encounters with Earth; only that the difference in oblateness between the two bodies is of little concern.

Given the small effect of ϵ on $K_{\ell m}$, it might be tempting to neglect the planetary oblateness when fitting $K_{\ell m}$ to data. However, the bottom pane of figure 16 demonstrates that doing so is invalid. This figure displays $K_{\ell m}$ as extracted by a fit assuming $\epsilon = 0$, but run on data generated with non-zero ϵ . The difference between the posterior means and true parameters are shown. Posterior uncertainties are also shown as bands. The figure shows that even for low (Moon-scale) oblateness, the fit results are inconsistent with the true $K_{\ell m}$ values, since $\Delta K_{\ell m} = 0$ is not contained in the 2σ band. This effect is much worse for large oblateness, growing to a difference on the order of 10^{-2} between the true and fit parameters for large oblateness. Therefore, accurately modelling central-body oblateness to high precision is essential for accurate estimation of fit parameters. For non-equatorial orbits, with $J_{22} \neq 0$, we also expect J_{22} to affect the accuracy of the fit results to a similar degree, with the additional requirement of using the correct asteroid orbital plane.

Note that J_{20} , the parameter studied in this section, has a slightly more general definition than oblateness. If the planet has a moon, the integral defining J_{20} (equation 5) can be extended to include this extra mass. Since J_{20} is a second moment, this effect is magnified for large distances of the mass from the central body centre of mass (though the effect is not quite quadratic because a_B also increases for large distances, and J_{20} is divided by a_B^2). This process is

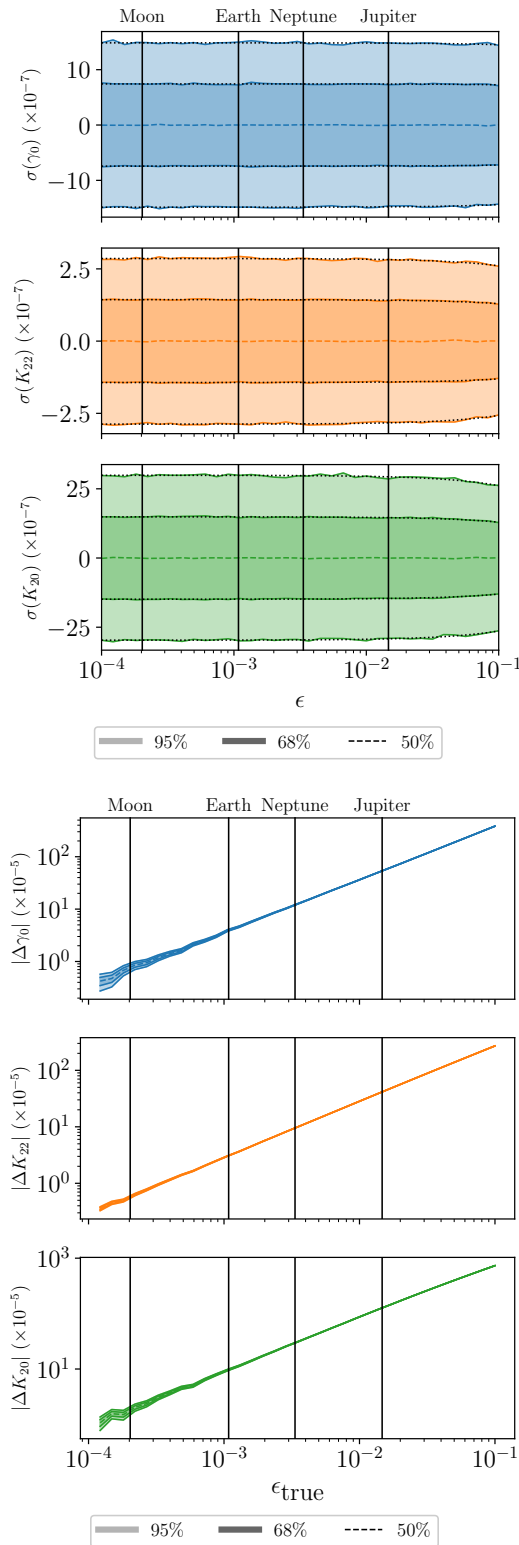


Figure 16. Top: 1 and 2σ confidence intervals for the first-order parameter posteriors as a function of oblateness ϵ . Linear best-fitting lines to σ (black, dotted) are plotted. Bottom: The difference between posterior means extracted from a zero-oblateness model and the true parameters given data with true oblateness $\epsilon_{\text{true}} \neq 0$. Also shown in both figures are the oblatenesses of reference Solar System bodies.

only valid when the asteroid never passes inside the moon's orbit.

As an order-of-magnitude estimate for this effect, two spherical objects with masses and radii of Earth and the Moon, separated by one Lunar distance, and both lying in the orbital plane has a combined $J_{20} = 0.25$. Extrapolating posterior uncertainty by the slopes of the best fit lines given earlier, this represents a decrease in $\sigma(K_{2m})$ by a factor of about one quarter.

This analysis suggests that large moons such as ours can improve fit quality, but further study of this effect is beyond the scope of this paper. Without a moon to inflate the oblateness of the central body, planetary oblateness does not significantly improve posterior uncertainty. However, correct representation of oblateness is essential to accurately estimate $K_{\ell m}$.

5 DENSITY DISTRIBUTIONS

Hitherto, we have only discussed the density moments $K_{\ell m}$ of the asteroid rather than the true density distribution $\rho(\mathbf{r})$. This is because only the density moments are observable by tidal torque interactions. However, by making sufficient assumptions about the density distribution, we can nevertheless estimate $\rho(\mathbf{r})$ from $K_{\ell m}$.

In this section, we outline three different assumptions which yield different types of density distributions for the same $K_{\ell m}$. One of them can be chosen, or a fourth created, depending on what features are desired to be represented in the density distribution. All three of these models assume that $a_{\mathcal{A}}$ and the asteroid shape is known (for example, by light curve or radar data). Uncertainty on this shape estimate is assumed to be small. The models then produce a density distribution $\rho(\mathbf{r})$ with uncertainty from $K_{\ell m}$ propagated to uncertainty in ρ .

In section 4, we were forced to fix $a_{\mathcal{A}}$ rather than fit for it because $a_{\mathcal{A}}$ is degenerate with scaling the K_{3m} components. However, $a_{\mathcal{A}}$ contains information about the density distribution as shown by its definition in equation 4. It might therefore be unreasonable to assume that it is exactly determined by light-curve or radar analysis. If $a_{\mathcal{A}}$ is too uncertain to be used as a known quantity when extracting density distributions from the moments, then the following models are flexible enough that the $a_{\mathcal{A}}$ constraint can be removed.

Note that, since the overall mass of the asteroid is not observable from tidal torque, we do not expect to measure ρ in an absolute sense. Only the differences in ρ across the body are measurable.

In section 5.1, we describe the general form our three models must take. Then in sections 5.2 to 5.4 we lay out each individually and compare them in section 5.5. In appendix D, we introduce a new model which does not assume that the asteroid shape is known, instead assuming that the density is constant. This allows us to compute the asteroid shape from $K_{\ell m}$.

5.1 General density model design

To set the shape of the asteroid, we assume that an indicator function $\mathbb{1}(\mathbf{r})$ has been determined such that $\mathbb{1}(\mathbf{r}) = 1$ inside the asteroid and 0 outside, where $\mathbb{1}(\mathbf{r})$ is defined in some

frame whose orientation with respect to Earth is known. Since the asteroid rotates around its centre of mass during observations, we assume that the location of the centre of mass is also known in this frame, so that we can set it to be the origin.

We define a new coordinate system, the “hybrid frame,” which coincides exactly with body-fixed frame at the initial orientation of the asteroid assuming that the fit result for γ_0 is perfectly accurate. The orientation of the hybrid frame with respect to the inertial frame is therefore exactly known, so that $\mathbf{1}$ is also exact in the hybrid frame. The $K_{\ell m}$ components are known in the body-fixed frame which aligns with the hybrid frame up to uncertainty in γ_0 . We will solve for $\rho(\mathbf{r})$ in the hybrid frame given fit results $K_{\ell m}$ (known in the body-fixed frame) and the fixed a_A (equal in all frames).

The density moments defined in equation 3 are not linear in $\rho(\mathbf{r})$, but we may fix a_A at the value assumed during the fit, removing the non-linearity induced by division by a_A . Furthermore, since the system is independent of the total asteroid mass, we set μ_A equal to an arbitrary constant which makes equation 3 linear in $\rho(\mathbf{r})$. Similarly, the form of equation 4 guarantees that a_A^2 is linear in $\rho(\mathbf{r})$. Equation 4 and the $K_{00} = 1$ component of equation 3 can each be applied as constraints to enforce these choices of a_A^2 and μ_A .

Suppose that we restrict the number of degrees of freedom of $\rho(\mathbf{r})$ from infinity to m by explicitly defining some function $\rho(\mathbf{r}, \Theta)$ for an m -dimensional vector Θ which contains the free parameters of ρ . We will leave the explicit definition of $\rho(\mathbf{r}, \Theta)$ to the model descriptions below, but for now we assume that ρ is linear in Θ ; i.e.,

$$\rho(\mathbf{r}, \Theta) = \mathbf{B}(\mathbf{r}) \cdot \Theta \quad (23)$$

for a m -dimensional vector $\mathbf{B}(\mathbf{r})$. (\mathbf{B} need not be linear in \mathbf{r} .) Thus, the defining equations of a_A^2 and $K_{\ell m}$ are linear in Θ . We further assume that the model describes a way to reverse this equation, to write

$$\Theta = A\mathbf{K} \quad (24)$$

where A is a matrix. Here, we have arranged a_A^2 and $K_{\ell m}$ into a vector \mathbf{K} , which we say has n dimensions. The order of this arrangement is irrelevant, as long as it is kept consistent.

To propagate uncertainties from \mathbf{K} to Θ and therefore $\rho(\mathbf{r})$, we need the covariance matrix Σ_K for \mathbf{K} . First, assume that the hybrid frame is offset from the body-fixed frame by some small angle $\Delta\gamma$, which results from uncertainty in γ_0 . Then

$$K_{\ell m}^{\text{hybrid}} = e^{-im\Delta\gamma} K_{\ell m}^{\text{body-fixed}}. \quad (25)$$

by equation 12. Since $K_{\ell m}^{\text{body-fixed}}$ was obtained by an MCMC fit, a large set of posterior-distributed samples is available for $\Delta\gamma$ and $K_{\ell m}^{\text{body-fixed}}$, and the covariance matrix Σ_K can be computed statistically in the hybrid frame by applying equation 25 to the samples. Then, propagation of uncertainty guarantees that the covariance matrix of Θ is $\Sigma_\Theta = A\Sigma_K A^T$ and the density distribution and uncertainty on density distribution are equal to

$$\rho(\mathbf{r}) = \mathbf{B}(\mathbf{r})^T A \mathbf{K} \quad \sigma_\rho^2(\mathbf{r}) = \mathbf{B}(\mathbf{r})^T A \Sigma_K A^T \mathbf{B}(\mathbf{r}). \quad (26)$$

The purpose of a model is therefore to restrict the space of valid density distributions by defining the $m \times n$ -dimensional constant matrix A and the m -dimensional vector $\mathbf{B}(\mathbf{r})$ such that equations 24 and 23 are true. Then the

density distribution and its uncertainty are given by equation 26.

5.2 The “likelihood” model

A natural way to restrict the degrees of freedom of $\rho(\mathbf{r})$ is by defining a likelihood function \mathcal{L} on the density distribution and choosing the one distribution which maximizes likelihood and exactly reproduces \mathbf{K} . We call this method the “likelihood” model. This likelihood should not be confused with the likelihood of equation 21, which was a function of the spin data, not the density distribution. The choice of the density \mathcal{L} is arbitrary, but the linearity of the model design outlined in the previous section will require a Gaussian likelihood.

To employ this likelihood method, we divide the asteroid into a square grid of $m \gg n$ elements, each of which is assumed to have uniform density $\rho_0 + \Theta_i$, where ρ_0 is constant across the asteroid and Θ_i is a local deviation. This defines the model function $\mathbf{B}(\mathbf{r})$, which is zeroed in all components except for the i th, where i is the index of the grid element that contains \mathbf{r} .

We use a likelihood of

$$\mathcal{L}(\Theta) = \prod_{i=1}^m \frac{1}{\sqrt{2\pi\sigma^2}} \exp\left(-\frac{\Theta_i^2}{2\sigma^2}\right) \quad (27)$$

with free parameters μ and σ . These parameters do not affect the location of the maximum, so we do not define them. Given this likelihood, the log likelihood is proportional to $-\|\Theta\|^2$. Minimizing the norm of Θ is therefore equivalent to finding the maximum likelihood.

Putting aside the problem of minimizing the norm, we use the linearity of equations 3 and 4 to write $\mathbf{K} = M\Theta$, where the i th entry of every row of the $n \times m$ matrix M is the integral presented in equation 3 or 4, evaluated over the i th finite element. We want to solve $\mathbf{K} = M\Theta$ for Θ to match equation 24, which we do via the Moore-Penrose inverse. Since $m > n$, the Moore-Penrose inverse of M is

$$A = M^+ = M^*(MM^*)^{-1} \quad (28)$$

where M^* is the adjoint of M . The vector $\Theta = M^+\mathbf{K}$ is guaranteed to solve $\mathbf{K} = M\Theta$, and by the properties of the Moore-Penrose inverse, this Θ also happens to minimize the norm of all possible Θ that satisfy the equation. Thus, defining $A = M^+$ also minimizes \mathcal{L} and fully defines the model.

Note that this model is fast to compute; assuming fast matrix multiplication, the matrix inversion of equation 28 is fast because MM^* is an n -dimensional square matrix, which is very small compared to the number of finite elements m .

5.3 The “harmonic” model

We now explore a model that seeks to restrict the space of allowed density distributions a different way: we allow only the density distributions with zero Laplacian: $\nabla^2\rho = 0$ inside the asteroid (the harmonic distributions). We therefore call this model the “harmonic” model. The expansion of a harmonic function in spherical coordinates is given by

$$\rho(\mathbf{r}) = \sum_{\ell m} \Theta_{\ell m} \frac{R_{\ell m}^*(\mathbf{r})}{a_A^\ell} \quad (29)$$

where the terms which lead to $\rho \rightarrow \infty$ at the origin have been removed and $\Theta_{\ell m}$ are free (complex) parameters. Since ρ is real, we have $\Theta_{\ell m} = (-1)^m \Theta_{\ell, -m}^*$. By setting a maximum on ℓ , we restrict the number of degrees of freedom to $(\ell_{\max} + 1)^2$. Choosing the same maximum ℓ as the maximum ℓ for the $K_{\ell m}$ moments, we have $m = n - 1$ coefficients $\Theta_{\ell m}$ which can be stacked into an m -dimensional vector Θ .

Inserting equation 29 into equations 3 and 4, we get

$$K_{\ell' m'} = \sum_{\ell m} \frac{1}{\mu_A a_A^{\ell'} a_A^\ell} \Theta_{\ell m} \int_A d^3 r R_{\ell m}^*(\mathbf{r}) R_{\ell' m'}(\mathbf{r}). \quad (30)$$

This is an over-determined matrix equation $\mathbf{K} = M\Theta$, where M is an $n \times m$ matrix. The Moore-Penrose inverse can therefore be used again to find an inverse $A = M^+$ which yields approximately correct Θ (approximate in that the norm of the error vector between \mathbf{K} and $M\Theta$ is minimized). However, the form of the inverse changes due to the equation being overdetermined:

$$A = M^+ = (M^* M)^{-1} M^* \quad (31)$$

In the special case where the asteroid is a sphere of radius R , the matrix defined by equation 30 is diagonal, with entries

$$M_{\ell m; \ell' m'} = \frac{4\pi R^3}{\mu_A} \frac{R^{2\ell}}{a_A^{2\ell}} \frac{\delta_{\ell\ell'} \delta_{mm'}}{(4\ell^2 + 8\ell + 3)(\ell - m)!(\ell + m)!}. \quad (32)$$

A non-spherical perturbation will introduce small off-diagonal entries to M . This diagonal represents another interpretation of the physical meaning of $K_{\ell m}$; they are directly proportional through this form of M and the matrix equation $\mathbf{K} = M\Theta$ to the coefficients of the spherical harmonic expansion of the asteroid density in the case of a spherical asteroid.

5.4 The “lumpy” model

The above two simple models produce smooth density distributions that generally extend non-uniformly over large regions. In this section, we define a more complicated model which identifies discrete regions differing from the overall density of the asteroid to best fit the measured density moments. We call this model the “lumpy” model.

Suppose the asteroid contains N “lumps” of uniform mass μ_i displaced by distance \mathbf{x}_i from the asteroid centre of mass and superimposed on a constant-density overall asteroid shape which is known in the form of $\mathbf{1}(\mathbf{r})$. For simplicity, we assume that all N regions are ellipsoids with d independent axis lengths. For example, $d = 3$ corresponds to an asymmetric ellipsoid, $d = 2$ corresponds to a symmetric ellipsoid, and $d = 1$ corresponds to a sphere. Recall that $\mathbf{1}(\mathbf{r})$ is known in the hybrid frame where the origin is the centre of mass of the asteroid. The displacement of the shape centroid from the centre of mass, which is the opposite of the net displacement of the discrete regions, is therefore observable from light curve analysis. The model therefore has $3(N - 1)$ positional degrees of freedom, along with N degrees of freedom for μ_i , Nd shape degrees of freedom, and 0, 2 N , or $3N$ rotational degrees of freedom for $d = 1, 2$, or 3 respectively. The sum of these degrees of freedom are displayed in table 3. These degrees of freedom should be compared to the known density moments and a_A , of which there are $(\ell_{\max} + 1)^2 + 1$. However, three of these are the

	N		
	1	2	3
1	2	7	12
2	5	13	21
3	7	17	27

Table 3. Total degrees of freedom D as a function of N , the number of lumps modelled, and d , the number of independent axis lengths considered for each lump. The configurations with $D \leq$ the six known parameters not including K_{3m} are coloured black, and with $D \leq$ the 13 parameters including K_{3m} parameters are coloured gray.

centre of mass of the asteroid which is guaranteed to be correct, and one is the unconstrained total mass so the total number of known parameters is $(\ell_{\max} + 1)^2 - 3$, which is 13 when the second-order density moments are known and six when only K_{2m} are known. We assume that the degrees of freedom of this lumpy model are always fewer than the number of \mathbf{K} known, so that the model is overdetermined.

The net $K_{\ell m}$ components of such an ensemble obey

$$K_{\ell m} = K_{\ell m}^{i0} + \sum_{i=1}^N K_{\ell m}^{i1} \quad a_A^2 = a_0'^2 + \sum_{i=1}^N a_i'^2 \quad (33)$$

where $K_{\ell m}^i$ and a_i^2 obey the same definition as $K_{\ell m}$ in equation 3 and a_A in equation 4 respectively, but integrated over the i th lump. Crucially, note that we set normalizing factors $1/(\mu_A a_A^\ell)$ and $1/\mu_A$ in equations 3 and 4 equal to the values for the entire asteroid, not their counterparts for each lump. The zero-indexed parameters indicate the moments of the uniform-density asteroid medium surrounding the lumps. The prime in equation 33 denotes that the moments are calculated in the hybrid frame, with its origin at the asteroid centre of mass.

We can relate the primed moments to the moments calculated relative to each lump’s centre of mass via the translation rules for solid spherical harmonics:

$$\begin{aligned} K_{\ell m}^{i1} &= \sum_{\ell' m'} (-1)^{\ell - \ell'} R_{\ell - \ell', m - m'}(\mathbf{x}_i) K_{\ell' m'}^i \\ a_i'^2 &= a_i^2 + x_i^2 \frac{\mu_i}{\mu_A} \end{aligned} \quad (34)$$

from Ref. van Gelderen (1998). The dummy indices ℓ', m' should only be summed over values in which $\ell - \ell' \geq 0$ and $|m - m'| \leq \ell - \ell'$. Here, μ_i is the added mass of lump i , while $K_{1m} = 0$ and K_{2m} incorporate the lump’s orientation and moment of inertia ratios. Its volume is constrained by a_i^2 . These values map directly onto an ellipsoid shape via equations 7, so that if $K_{\ell m}^i$, a_i^2 , μ_i , and x_i are known, then the density distribution of the asteroid is known.

Note that if \mathbf{x}_i is known, then equation 34 are linear in $K_{\ell m}^i$ and a_i^2 . Therefore, if we define Θ to contain K_{2m}^i and a_i^2 for all i in some order, then equations 34 and 33 define a matrix equation $\mathbf{K} = \mathbf{C} + M\Theta$ which can be solved by setting A equal to the Moore-Penrose inverse of M (equation 31, since Θ is overdetermined). Note that the \mathbf{C} term of this equation came from the expansion of $K_{\ell m}^{i0}$ and $a_0'^2$, which is written in terms of the already-known displacement of the asteroid surface from its centre of mass and the already-known surface shape.

This model’s strategy will be to choose \mathbf{x}_i and μ_i via a non-linear process, then fit for the values $K_{\ell m}^i$ and a_i^2 using

the linear format described in section 5.1. The constraints on \mathbf{x}_i is

$$\sum_{i=1}^N \mathbf{x}_i \mu_i + \mu_0 \mathbf{x}_0 = 0 \quad (35)$$

where \mathbf{x}_0 is the known displacement of the centroid of the asteroid model from the centre of mass. There are also additional constraints, such as that \mathbf{x}_i should lie inside the asteroid which can be enforced manually. The overall mass of the asteroid is $\mu_A = \mu_0 + \sum_{i=1}^N \mu_i$, and has been set, so we may eliminate μ_0 from equation 35. The constraint is now a function of μ_i and \mathbf{x}_i for $i \geq 1$. The matrix equation defining M is overdetermined, but we would like it to have a solution nevertheless. We therefore solve for \mathbf{x}_i and μ_i to yield an M with close solutions. This is done by minimizing

$$|(M(\mathbf{x}_i, \mu_i) M^+(\mathbf{x}_i, \mu_i) - \mathbf{1})(\mathbf{K} - \mathbf{C})|^2. \quad (36)$$

which is the difference between \mathbf{K} resulting from the model and the true \mathbf{K} . Here, $\mathbf{1}$ is the identity matrix. Then $A = M^+$ defines the model. We cannot define $\mathbf{B}(\mathbf{r})$ such that $\rho(\mathbf{r})$ is linear in \mathbf{B} , but uncertainty on $K_{\ell m}^i$ can still be evaluated as Σ_Θ and these can be converted into uncertainties in the dimensions and orientations of the lumps. If the resulting density distribution is somehow excluded (it predicts negative density distributions, the lumps extend outside the asteroid, etc.), then another minimum of equation 36 can be used, or another combination of N and d listed in table 3.

5.5 Comparisons between density models.

To test the properties of the three density models defined above, we simulate several asteroids with different shapes and density distributions on a close Earth encounter with the reference asteroid orbital and observational parameters. Density moments are extracted via our fit process and density distributions extracted by the three above methods. Below, we compare the resulting distributions to understand the performance of the extraction methods.

5.5.1 Uniform density test asteroids

First, we simulate several asteroids with uniform density distributions and ask whether a uniform distribution is recovered. The shapes we use are the symmetric and asymmetric reference ellipsoids, a “dumbbell” (two spheres of equal radius conjoined such that the surface of one intersects the centre of the other), and a tetrahedron. We use these shapes as rough approximations of potential shape types (i.e., a contact binary for the dumbbell, a polyhedron for the tetrahedron), but also to demonstrate the density models’ efficacy on sharp corners. The extracted distributions for all three models are shown in figure 17. Also in each figure is $\Delta K_{\ell m}$, the squared magnitude of difference between the fitted density moments and the density moments of the final distribution. This difference is non-zero due to numerical error in the likelihood model case, but for the harmonic and the lumpy models, they express the degree to which the extracted moments cannot be represented with harmonic or lumpy distributions respectively.

From figure 17, it can be seen that the likelihood and harmonic models produce mostly the same density distributions. This is generally true for uniform density asteroids, which have harmonic density distributions. Consequentially, $\Delta K_{\ell m}$ is low for the harmonic model. This similarity lends confidence that the models produced are truly representative of the asteroid since they are produced via two independent methods.

The asymmetric and dumbbell asteroids produce distributions whose non-uniformity is limited to a factor of 2 or less for the harmonic and likelihood models. This non-uniformity is driven by error in the estimates of the density moments. Note that most of the asteroid has density close to one in both cases, with the factor of two reached only by small regions. The lumpy model yields a much more uniform distribution, because it is designed to produce uniform lumps. Note that its uncertainty $\Delta K_{\ell m}$ is usually large, both because the model is severely overdetermined (it has 2 degrees of freedom) and because the lump found extends outside the asteroid, violating the assumptions of the model. This is a sign that the lump found does not really exist inside the asteroid.

The symmetric and tetrahedral asteroids are less-well represented by the density distribution model results. In both cases, the likelihood and harmonic models produce sometimes-negative distributions, and non-uniformity is especially large in the tetrahedral case. This is not the fault of the density models, but rather because both of these asteroids have $K_{22} = 0$ and (as discussed in section 4.3), this leads to degeneracy in γ_0 and inflated uncertainty in the density moments. In the tetrahedral case, the problem is worsened because $K_{20} = 0$ as well, so that torque is dominated by the small and ill-constrained K_{3m} components.

Uncertainty in each distribution was calculated but not shown. The size of uncertainty is such that the density distribution is consistent with uniform at most points for all models (within 1–2 σ), with a small number of low-uncertainty regions that are less consistent with uniform. Uncertainty is generally larger towards the edges of the distribution, both for these shapes and for the shapes shown in the following sections.

From these examples, we may draw the conclusions that all three models produce density distributions generally consistent with uniform for uniform asteroids. The most likely distributions (i.e., the ones shown in the figures) are themselves mostly uniform, but can still produce non-uniformities as large as a factor of 2 in certain regions due to uncertainty in $K_{\ell m}$. Asymmetric asteroids such as the dumbbell and the asymmetric reference asteroids yield the best results because they have $K_{22} \neq 0$ and therefore do not suffer from degeneracy in initial orientation. Finally, the lumpy model can generally be ruled out in these cases because it produces unphysical results.

If desired, the parameters of the models can be reduced to only fit the K_{2m} density moments; this will produce exactly uniform distributions, since it is equivalent to assuming $K_{3m} = 0$. However, doing so ignores the observational insight we gain from our fits to K_{3m} , so it is only valid when K_{3m} are too poorly constrained to be used.

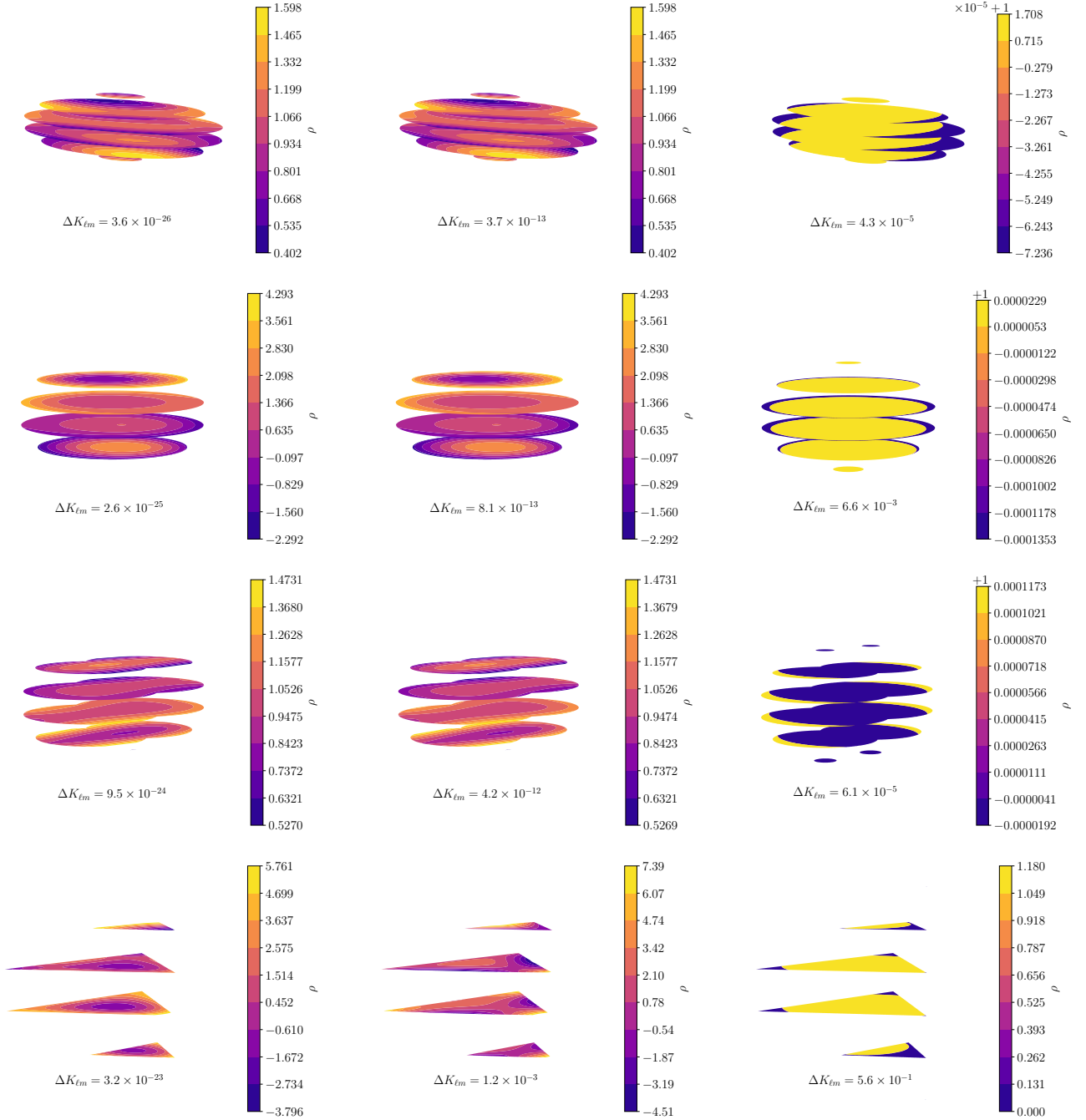


Figure 17. Density distributions extracted by the likelihood (left), harmonic (middle), and lumpy with $d = N = 1$ (right) models from data generated for a uniform-density asteroid. The asteroid shapes are, from top to bottom, the reference asymmetric ellipsoid, the reference symmetric asteroid, the dumbbell model, and a tetrahedron. Density is normalized so that mean density is one. The same distance scale is used in all figures.

5.5.2 Spherical shape test

We test the sensitivity of the density distributions to incorrect estimates for the shape of the asteroid by obtaining density moments from an ellipsoidal asteroid encounter and extracting density distributions assuming a spherical shape. We do this for the asymmetric and symmetric reference asteroids, with density distributions shown in figure 18.

Both the likelihood and harmonic models are accurate

in that $\Delta K_{\ell m}$ is low, and they both produce similar distributions as in the previous section. However, now they both produce negative density distributions for both asteroid shapes. (In the previous section, only the symmetric model did.) This is a signal that the shape model is incorrect, and indeed the density distribution allows us to determine exactly how the shape model is wrong. In the asymmetric ellipsoid case, the density distribution is small (even negative) at large $|z|$ (top and bottom of the figure). The density is large at

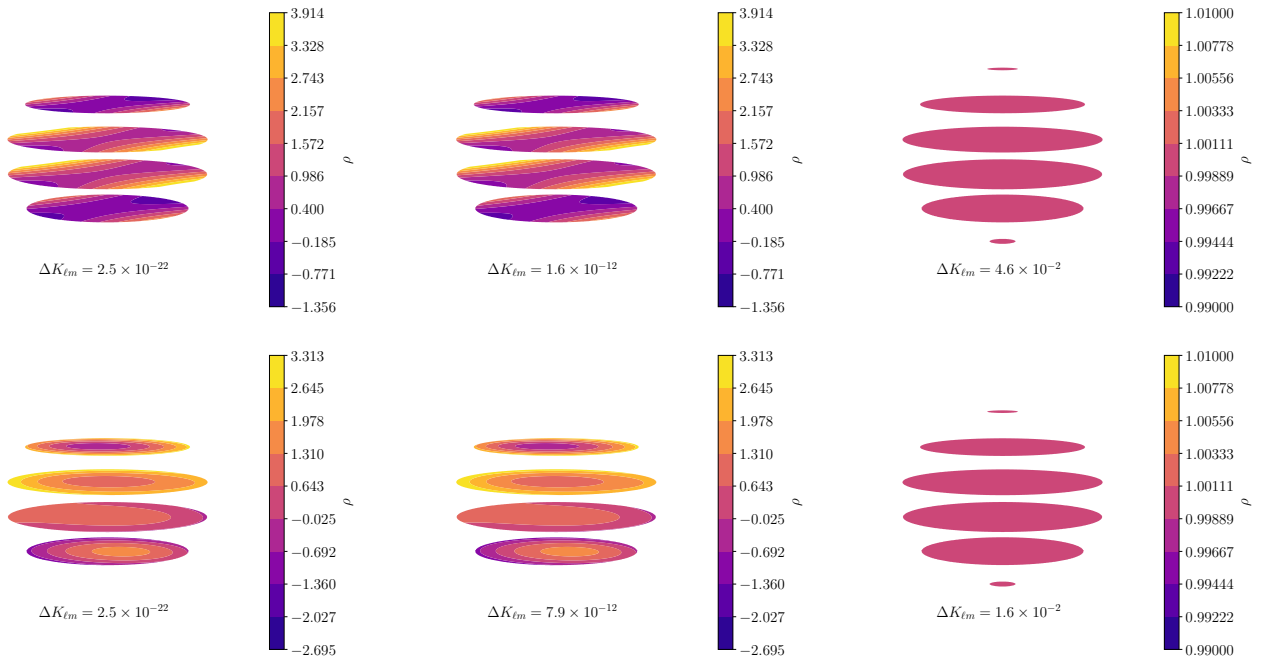


Figure 18. Density distributions extracted by the likelihood (*left*), harmonic (*middle*), and lumpy with $d = N = 1$ (*right*) models from data generated for a uniform-density asteroid. The original asteroid shapes were the reference asymmetric (*top*) and symmetric (*bottom*) ellipsoids. In both cases, the density distributions have been extracted assuming a spherical shape. Density is normalized so that mean density is one. The same distance scale is used in all figures.

large $|y|$ (front right and back left in the figure). Comparison with the asymmetric reference asteroid depicted in figure 17 shows that the low-density region is outside the true asteroid shape, and the high-density region is inside. In other words, the shape can be corrected by extending it where density is large and retracting it where density is low.

A similar statement is true for the symmetric ellipsoid case in that density is low near the poles, but this time the regions with large density are evenly distributed around the equator, indicating the symmetry of the original asteroid.

The lumpy model produces lumps so large that they dominate the asteroid, predicting uniform distribution with $K_{\ell m} = 0$ for $\ell \geq 1$. The error in density moments $\Delta K_{\ell m}$ is therefore very large, equal to the sum of $|K_{\ell m}|$ for the original asteroids, making it clearly a poor model.

In short, severely incorrect shape estimates can be caught for all three models by negative predicted densities or by the failure of the density distribution model to match the extracted density moments. The shape can be corrected by extending it where the density distribution is high and retracting it where the density distribution is low.

5.5.3 Nonuniformity test

We also test several non-uniform density asteroids and compare the generated density distributions for all three models to see if the non-uniformities are recovered. We consider two asteroids, one with mass concentrated in the middle, and one with mass concentrated around the edges. (Specifically, the mass distribution follows a spherically symmetric exponential $\rho(r) \propto e^{\pm r^2/a_A^2}$). To prevent the problems seen in previous sections when a symmetric asteroid is simulated,

we set the shape of the asteroids to the asymmetric reference asteroid. The extracted density distributions are shown in figure 19

For these non-uniform asteroids, the likelihood and harmonic model do not coincide, as can be seen by comparing the density distributions and the fact that $\Delta K_{\ell m}$ is much larger for the harmonic distribution (indicating that the true density distribution is not harmonic). However, the two models do give similar results. Comparing the centre-weighted asteroid and the edge-weighted asteroid distributions, one can see that the centre-weighted case indeed places more mass in the centre of the asteroid shape for the harmonic and likelihood models, while the edge-weighted asteroid places mass at the edges.

Though these general trends in mass placement arrived at by both the likelihood and harmonic models are accurate, the precise density distributions are inaccurate because they predict negative densities. This might be addressed for the likelihood model by selecting a likelihood that strongly disfavours negative densities, such as a log-normal distribution. A log-normal likelihood however would no longer yield a linear model, so we do not use one here.

Figure 19 shows that the lumpy model places one large lump of greater density than the surrounding medium for the centre-weighted asteroid and less density for the edge-weighted asteroid, as expected. Greater error is incurred in $\Delta K_{\ell m}$ in this lumpy model than for the harmonic and likelihood models due to the lumpy model's crudeness, but the lump gives a good qualitative estimate of the density distribution of the asteroid which is useful for interpreting the other two models. This fact demonstrates that it can be illustrative to run the models with reduced degrees of freedom

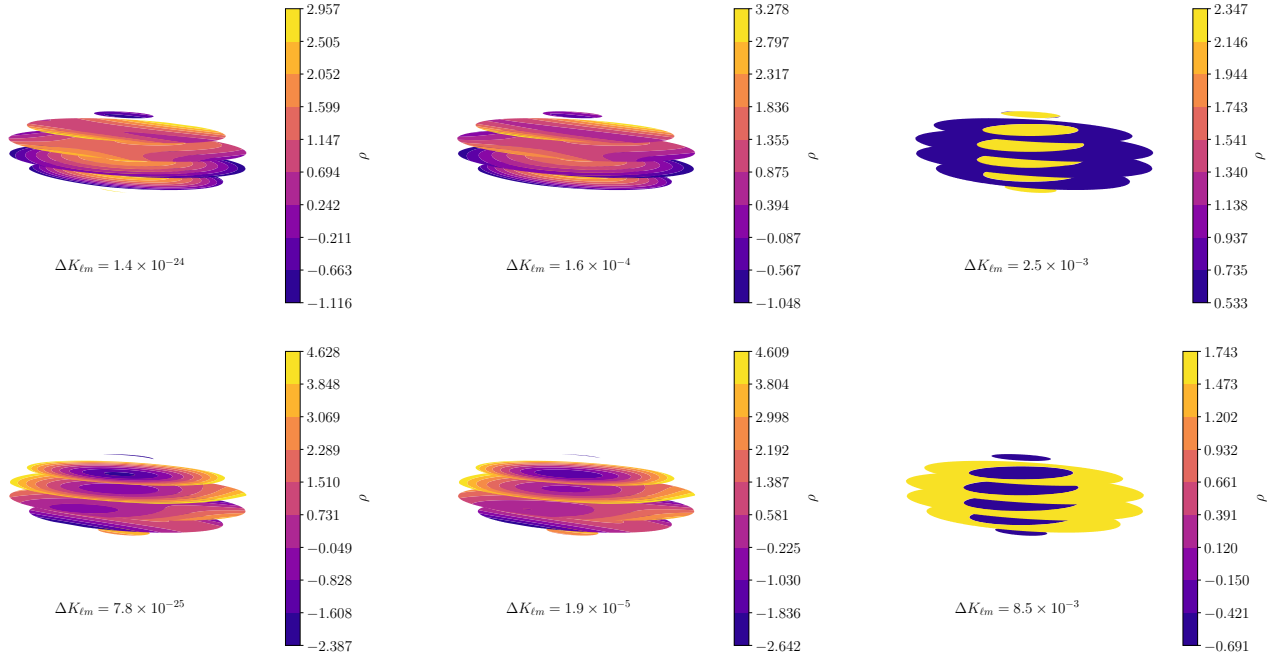


Figure 19. Density distributions extracted by the likelihood (*left*), harmonic (*middle*), and lumpy with $d = N = 1$ (*right*) models from data generated for non-uniform-density asteroids with mass concentrated in the middle (*top*) and the edges (*bottom*). Density is normalized so that mean density is one. The same distance scale is used in all figures.

for the sake of simplicity, even if doing so yields less accurate distributions.

The lumpy model has one caveat that has not yet been mentioned, which applies for $N = d = 1$ if (1) the centre of mass of the asteroid is the centroid of the asteroid shape and (2) the density moments of the asteroid shape are proportional to the fitted density moments. (1) guarantees that the lump will be placed at the origin and therefore will not contribute to $K_{\ell m}$ for $\ell \geq 1$, and (2) guarantees that the mass of the asteroid shape will be chosen such that the shape density moments exactly match the fitted density moments. The lump radius will then be set to zero because the fitted density moments are already matched. This zero-radius-lump result will occur even if the true density distribution has a large-radius lump at the origin. The lump model will therefore fail to recognize the lump in the true density distribution.

An example of this caveat applied is an elliptical lump inside an elliptical asteroid similar to the ones above. This is why, in the centre-weighted and edge-weighted density distributions, we specifically chose a spherically symmetric density distribution for our ellipsoidal asteroid shape, rather than an a distribution that conforms to the asteroid shape.

5.5.4 Lump test

Finally, we test an asteroid with a discrete change in density distribution (for example, a boulder), of the kind that the lumpy model is designed to detect. We place a spherical mass of density six times the density of the surrounding medium inside the asymmetric reference asteroid, slightly displaced along $\hat{\mathbf{y}}$. The rest of the asteroid we set to uniform density.

The density distributions found by the three model for this asteroid are shown in figure 20.

We see from figure 20 that the harmonic and likelihood model fail completely to recover the presence or location of the lump. There appears to be a slight increase in density at roughly the correct location for both models, but this is a small effect Like figure 19, we see that the harmonic and likelihood models do not agree exactly, and the failure of the harmonic model to exactly reproduce $K_{\ell m}$ suggests that the true distribution is not harmonic.

The failure of these models to find lumps is expected, since $K_{\ell m}$ is most sensitive to non-uniformities of characteristic size $\pi/(\ell + 1)$ radians in the polar direction, and $2\pi/(|m| + 1)$ in the azimuthal direction by the definition of $Y_{\ell m}$. This lump is too small to be resolvable by K_{3m} , so we do not expect most models to find it.

However, the lumpy model computes the location and density of the mass very well. Some inaccuracies are induced by the uncertainty in K_{3m} , which changes the minimum of equation 36 such that the lump is displaced by 9 m along $\hat{\mathbf{y}}$ from where it should be. This in turn causes a 70 m inaccuracy in the lump's radius. Nevertheless, the accuracy is still good compared to other models, and we conclude that the lumpy model is capable of recreating the location of lumps (except for the caveat mentioned in the previous section for distributions with $K_{\ell m}$ proportional to the asteroid shape's moments). But the ability of the lumpy model to place a lump does not guarantee the lump to actually exist, as was seen in the other asteroid distributions analysed here.

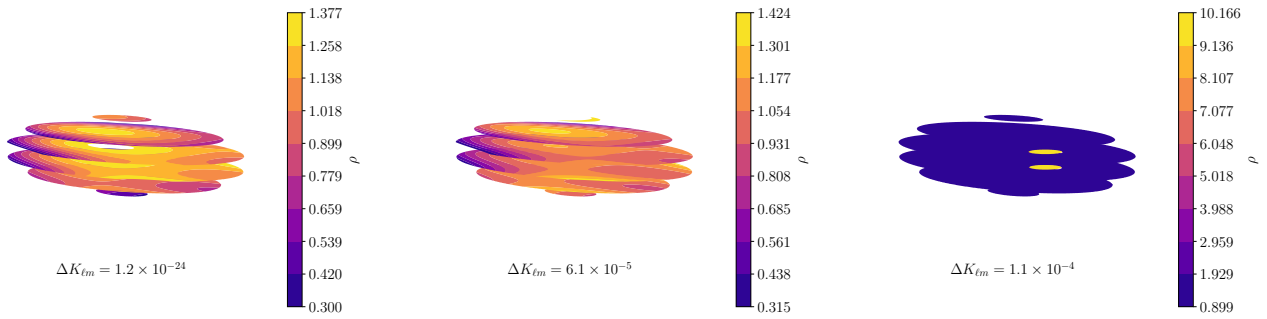


Figure 20. Density distributions extracted by the likelihood (*left*), harmonic (*middle*), and lumpy with $d = N = 1$ (*right*) models from data generated for an asteroid with an off-centre lump. Density is normalized so that mean density is one. The same distance scale is used in all figures.

6 CONCLUSIONS

We assess the feasibility of extracting density moments and density distributions for a general asteroid encounters, and ask what encounter properties are necessary to obtain the most information about asteroid density.

We derived a novel, arbitrary-order equation for the tidal torque experienced by an asteroid during an encounter with a planet of arbitrary shape and mass distribution. The tidal torque equation (equation 15) revealed that the rotational velocity of the asteroid over time depends strongly on $K_{\ell m}$ and the initial orientation.

We built a fast simulation for an asteroid encounter, truncating the equation at second-order, and used the simulation to extract first- and second-order density moments from synthetic spin pole data via a Markov Chain Monte Carlo fit. We observe the following general properties of the moments:

(i) The second-order moments K_{3m} are generally a factor of $\frac{a_A}{r_p}$ more uncertain than the first-order moments, where a_A is the asteroid radius and r_p is the perigee distance. For our reference asteroid, this fraction was about 10^{-5} .

(ii) Of the seven second-order moments, those that measure small-scale variations in density (i.e., $|m|$ is large) are generally less uncertain. It is often possible to measure $K_{3|m|}$ for large m even when K_{30} is not resolved.

(iii) The oblateness of the central body cannot be ignored without generating incorrect density moment estimates, but a non-zero oblateness does not greatly increase the precision of the extracted moments except perhaps when a moon is present.

We assessed the posterior uncertainty generated by the fit process by adjusting eleven parameters of an asteroid on an Earth encounter. The main conclusions are listed below.

(i) Highly precise rotational velocity data is required to produce precise second-order moments. Especially the uncertainty on the asteroid rotational period must be small compared to the uncertainty on asteroid spin pole.

(ii) Large a_A is required for K_{3m} resolution, though the size of a_A has no effect on K_{2m} . The threshold on a_A for the reference asteroid was ~ 700 m for K_{30} and ~ 50 m for K_{33} .

(iii) A close encounter is vital for accurate second-order moment extraction, though some of the second-order mo-

ments can still be required for more distant encounters, extending to about a third of a Lunar distance for the reference asteroid.

(iv) This model will yield inflated uncertainties if the asteroid is rotationally symmetric around its rotating spin axis. In this case, a different parametrization should be used.

(v) If the asteroid rotational period is too small, the asteroid will not tumble after perigee. This inhibits the precise determination of K_{2m} , though K_{3m} are largely unaffected. For the reference asteroid, the threshold was about 4 hours (although K_{30} will become unresolved at for periods smaller than 8 hours). For similar reasons, initial rotational velocities orthogonal to the orbital plane or in the plane and perpendicular to the perigee vector will yield poor-quality fits, though the spin pole effect is smaller than the effect of rotational period.

(vi) The cadence of observation should be shorter than about 30 minutes (except K_{30} will become unresolved for cadence longer than 10 minutes). Gaps of data can appear, specifically at perigee, but only for a little over an hour given 2 minute cadence before the posterior uncertainty greatly increases.

If some of these conditions are not met, the first-order K_{2m} moments may still be resolvable.

Finally, we present three fast, linear methods for extracting density distributions (together with uncertainties) from the density moments and the shape of the asteroid as obtained by light-curve analysis. The extracted density distributions largely are consistent with the true distributions in all cases we tested. Slight adjustments to K_{3m} dramatically change the overall distribution, so that they are not very precise. Indeed, the models sometimes predict negative density (though more complicated models could be made not to). Errors in the shape estimate of the asteroid also distort the density distribution, but the resulting distributions provide hints as to exactly where the shape is incorrect. Large-scale properties of the asteroid's true distribution, such as whether the mass is located in the middle or on the edges, are often observable. Two of the models presented (the harmonic and lumpy models) are flexible in their number of parameters, so that if only these large-scale properties are necessary, a small set of parameters can be chosen to prevent over-fitting.

In the appendices, we answer more specific questions

that might arise about the behaviour of the tidal torque system and the fit process.

ACKNOWLEDGEMENTS

We warmly thank Emmanuel Jehin, Maxime Devogele, and Marin Ferrais for meeting with the authors to discuss this work, and pointing out possible future directions to take it. JTD would like to thank the Massachusetts Institute of Technology Undergraduate Research Opportunities Program (MIT UROP) office for funding his work for many semesters, and their flexibility in funding students from departments other than the source of funding. The work of JdW was funded by **JTD: Who funds Julien?**. Much of the computation behind this paper was executed on MIT Supercloud's facilities.

DATA AVAILABILITY

The code used to generate data, fit density moments to it, and extract density distributions from the moments is available on [GitHub](#), or by contacting JTD.

REFERENCES

- Ashenberg J., 2007, *Celestial Mechanics and Dynamical Astronomy*, 99, 149
- Baxansky A., Kiryati N., 2007, *Pattern Recognition*, 40, 756
- Benson C. J., Scheeres D. J., Moskovitz N. A., 2020, *Icarus*, 340, 113518
- Berthier J., et al., 2020, *Icarus*, 352, 113990
- Boué G., Laskar J., 2009, *Icarus*, 201, 750
- DeMartini J. V., Richardson D. C., Barnouin O. S., Schmerr N. C., Plescia J. B., Scheirich P., Pravec P., 2019, *Icarus*, 328, 93
- Descamps P., et al., 2020, *Icarus*, 345, 113726
- Foreman-Mackey D., Hogg D. W., Lang D., Goodman J., 2013, *Publications of the Astronomical Society of the Pacific*, 125, 306
- Gao F., Han L., 2012, *Computational Optimization and Applications*, 51, 259
- Giorgini J., Benner L., Nolan M., Ostro S., 2005, in *AAS/Division of Dynamical Astronomy Meeting# 36*. pp 02–01
- Giorgini J. D., Benner L. A., Ostro S. J., Nolan M. C., Busch M. W., 2008, *Icarus*, 193, 1
- Hirabayashi M., Kim Y., Brozović M., 2021, *Icarus*, 365, 114493
- Hou X., Scheeres D. J., Xin X., Mar 2017, *Celestial Mechanics and Dynamical Astronomy*, 127, 369
- Kaiser N., et al., 2002, in *Survey and Other Telescope Technologies and Discoveries*. pp 154–164
- Kwiecinski J. A., Krause A. L., Van Gorder R. A., 2018, *Icarus*, 311, 170
- Larson S., Brownlee J., Hergenrother C., Spahr T., 1998, in *Bulletin of the American Astronomical Society*. p. 1037
- Lee H.-J., et al., 2022.
- Makarov V. V., Goldin A., Tkachenko A. V., Veras D., Noyelles B., 2022.
- Moskovitz N. A., et al., 2020, *Icarus*, 340, 113519
- Naidu S. P., Margot J.-L., 2015, *The Astronomical Journal*, 149, 80
- Pater D. I., Lissauer J. J., 2015, *Planetary sciences*, 2 edn. Cambridge University Press
- Paul M. K., 1988, *Celestial mechanics*, 44, 49
- Pravec P., et al., 2014, *Icarus*, 233, 48
- Richardson D. C., Bottke W. F., Love S. G., 1998, *Icarus*, 134, 47
- Scheeres D., Ostro S., Werner R., Asphaug E., Hudson R., 2000, *Icarus*, 147, 106
- Scheeres D. J., Marzari F., Rossi A., 2004, *Icarus*, 170, 312
- Scheeres D., Benner L., Ostro S., Rossi A., Marzari F., Washabaugh P., 2005, *Icarus*, 178, 281
- Smalley K., Garradd G., Benner L., Nolan M., Giorgini J., Chesley S., Ostro S., Scheeres D., 2005, *International Astronomical Union Circular*, 8477, 1
- Souchay J., Souami D., Lhotka C., Puente V., Folgueira M., 2014, *Astronomy & Astrophysics*, 563, A24
- Souchay J., Lhotka C., Heron G., Herve Y., Puente V., Lopez M. F., 2018, *Astronomy & Astrophysics*, 617, A74
- Stokes G. H., Evans J. B., Viggh H. E., Shelly F. C., Pearce E. C., 2000, *Icarus*, 148, 21
- Valvano G., Winter O. C., Sfair R., Machado Oliveira R., Borderes-Motta G., Moura T., 2022, *Monthly Notices of the Royal Astronomical Society*, 510, 95
- Wright E. L., et al., 2010, *The Astronomical Journal*, 140, 1868
- Yu Y., Richardson D. C., Michel P., Schwartz S. R., Ballouz R.-L., 2014, *Icarus*, 242, 82
- van Gelderen M., 1998, in *The shift operators and translations of spherical harmonics*.

APPENDIX A: REFERENCE ASTEROID CONFIGURATIONS

Except when otherwise mentioned, we use the following asteroid encounter parameters. Many of the parameter choices are made to maximize the quality of observations (a close orbit, large asteroid, etc.) This is so that our uncertainties have room to grow; if the reference asteroid has low uncertainty, we would not be able to measure uncertainty increases as well when the encounter parameters are adjusted.

(i) An orbit around a spherical, Moonless Earth with 6 km s^{-1} excess velocity and perigee at 5 Earth radii. This orbit was chosen to roughly match that of 99942 Apophis [Giorgini et al. \(2005, 2008\)](#); [Smalley et al. \(2005\)](#), discovered on June 19, 2004 by R. A. Tucker, D. J. Tholen, and F. Bernardi. These orbital parameters correspond to an eccentricity of 3.88. The comparison to Apophis is complicated by the fact that Apophis is smaller than our $a_{\mathcal{A}}$ value, is tumbling [Pravec et al. \(2014\)](#), and may change slightly in physical properties due to tidal interaction during the encounter [Yu et al. \(2014\)](#); [Hirabayashi et al. \(2021\)](#). It therefore is not entirely comparable to our analysis.

(ii) An initial roll of $\gamma_0 = \pi/8$.

(iii) A cadence of 2 minutes and observational uncertainty of $\sigma_\theta = 0.01$ and $\sigma_\rho/\sigma_\theta = 10^{-5}$.

(iv) A rotational period of 9 hours, with the rotational velocity vector distributed between the $\hat{\mathbf{X}}$, $\hat{\mathbf{Y}}$, and $\hat{\mathbf{Z}}$ axes in a $1 : 2 : -2$ ratio.

(v) An asteroid with radius $a_{\mathcal{A}} = 1 \text{ km}$ and $K_{3m} = 0$. For K_{22} and K_{20} , we use two standard values: one with $(K_{22}, K_{20}) = (0, -0.097)$ and one with $(0.052, -0.202)$. Including the third point obtained by reflection $K_{22} \rightarrow -K_{22}$, these are the three points that minimize the mean distance between an arbitrary point in the allowed parameter space (equation 8) and these reference values. The first point is called the symmetric case because the corresponding uniform-density-ellipsoid model is rotationally symmet-

ric around \hat{z} . The second case and its reflection are called the asymmetric cases. Values of $(0.052, -0.202)$ have $a < b$ in the ellipsoid model, and the reflected value has $a > b$. If not specified, we use the $a < b$ case. Specifically, the asymmetric case has $a = 1140$ m, $b = 1839$ m, and $c = 565$ m, while the symmetric case has $a = b = 1411$ m and $c = 1008$ m.

We use the asymmetric ellipsoid in nearly all runs, due to the degeneracy induced in our model when $K_{22} = 0$.

APPENDIX B: THE CADENCE CUT-OFF

In section 4.4, we noted that posterior uncertainty as a function of observation cadence Δt appears to increase suddenly near $\Delta t \sim T_{\text{cad}} = 30 - 40$ min. We mentioned that this cadence cut-off is likely a function both of the rotational period of the asteroid and the time spent near perigee. We study this cut-off in closer detail in this appendix.

We measure the dependence of the cadence cut-off on rotational period by varying the period P_ω and reproducing figure 11; i.e., we run many simulations of the changed P_ω with different cadences and plot the posterior fit uncertainty σ as a function of cadence Δt . Specifically, we use $P_\omega = 5$ hr and 20 hr, roughly double and half of the reference $P_\omega = 9$ hr. The resulting curves of $\sigma(\Delta t)$ are shown in figure B1, with each normalized so that their maximum values is 1 so that changes to σ induced by the change in P_ω that are not a function of Δt (i.e., those studied in section 4.7), are removed; they are irrelevant here.

We also wish to capture dependence on the time spent by the asteroid near perigee, but we do not wish to change the orbit shape or central body, because this may induce other effects that could also affect the cadence plot. Instead, we (un-physically) manipulate the speed at which the asteroid moves through the orbit. In one instance, the asteroid's path is artificially slowed by a factor of 2, which we denote as $t_{\text{spin}}/t_{\text{orbit}} = 0.5$; in the other instance, $t_{\text{spin}}/t_{\text{orbit}} = 2$, meaning that the orbit is sped up. This approach of changing the speed of the orbit is meant to approximate changes to T_p defined in equation 22. The posterior uncertainties for these two cases and the original case are shown as a function of Δt in figure B2. Again, σ is normalized so that Δt -independent variations are removed. The $t_{\text{spin}}/t_{\text{orbit}} = 2$ uncertainties begin to fill the prior distribution for large Δt for some parameters, which can be seen by discontinuous variation in the dotted line of figure B2.

Many of the curves in figures B1 and B2 show a cadence cut-off at $T_{\text{cad}} \sim 30 - 60$ min. Those that show no cut-off (i.e., they merely smoothly increase over Δt) may in fact exhibit a cut-off $T_{\text{cad}} > 60$ min, which is off the plot. By comparing $\sigma(\Delta t)$ for a specific parameter, we see that the dashed lines often (but not always) reach the cadence cut-off at lower Δt than the solid line. For example, in figure B1, this effect is especially clear for K_{22} , K_{33} , $\Im K_{22}$, and $\Re K_{31}$, but the opposite appears for $\Re K_{32}$. The dashed curves are significant in both figures because they represent larger σ cases ($P_\omega = 5$ hours, or $t_{\text{spin}}/t_{\text{orbit}} = 2$); section 4.7 reveals that fast rotators lead to larger σ , and $t_{\text{spin}}/t_{\text{orbit}} > 1$ leads to larger σ because of the presence of less perigee data. It therefore appears that small P_ω and small times spent at perigee move the cadence cut-off to smaller T_{cad} .

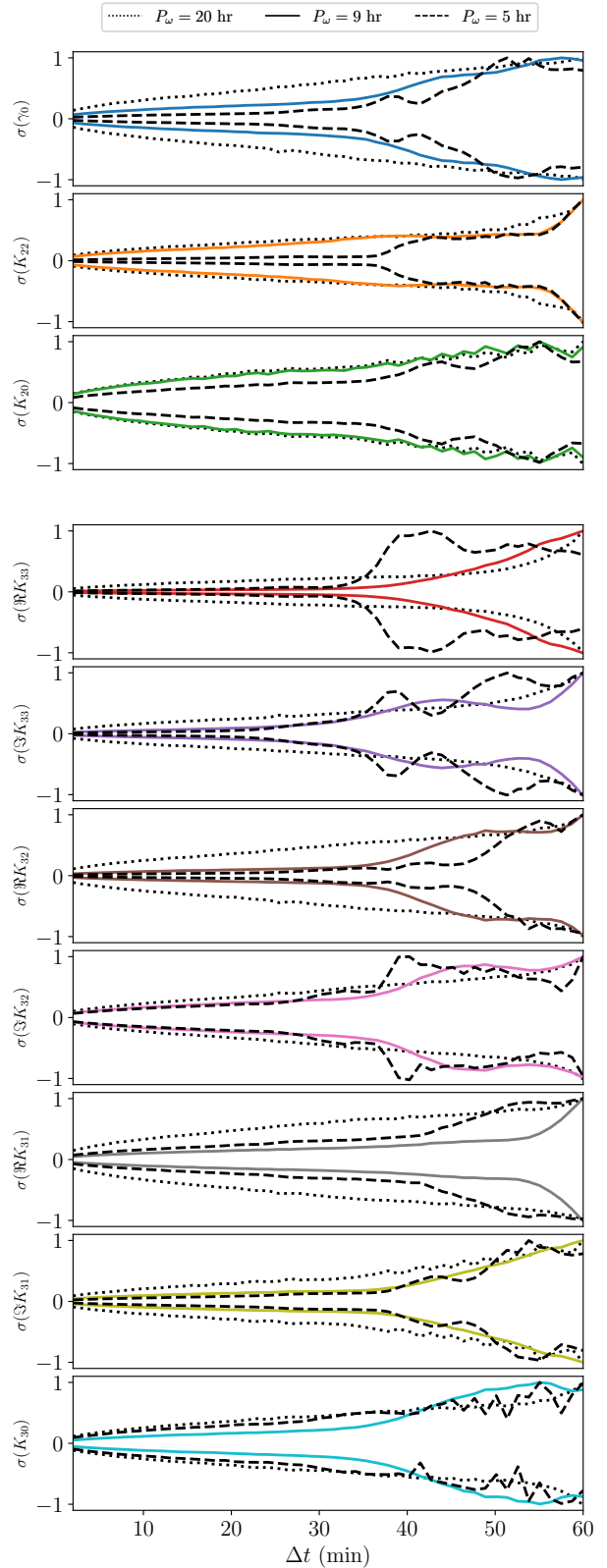


Figure B1. 1σ confidence intervals plotted as a function of cadence Δt for periods of 9 hr (the reference asteroid, solid coloured lines), and 5 hours (dotted lines), and 20 hours (dashed lines). Confidence intervals have been normalized for the sake of comparison, so that the maximum for each curve is 1.

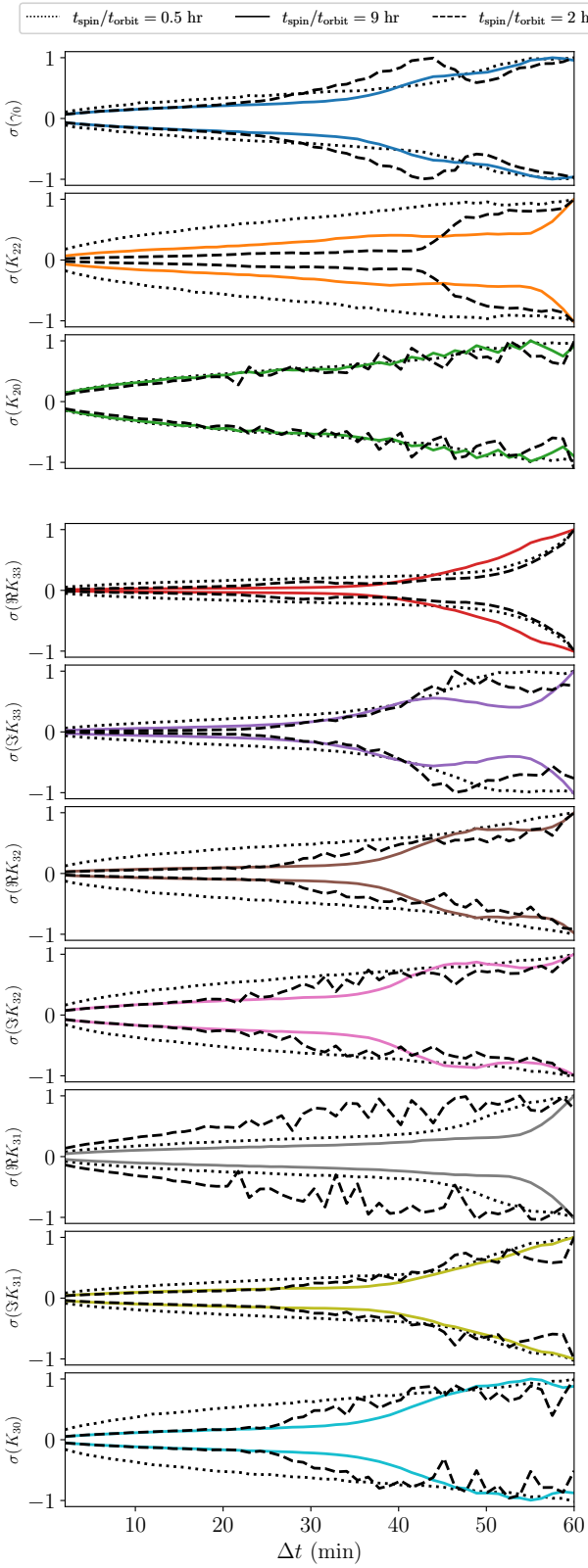


Figure B2. 1σ confidence intervals plotted as a function of the orbit time scaling $t_{\text{spin}}/t_{\text{orbit}}$ for no scaling (the reference asteroid, solid coloured lines), time doubling (dotted lines), and halving (dashed lines). See text for the definition of $t_{\text{spin}}/t_{\text{orbit}}$. Confidence intervals have been normalized for the sake of comparison, so that the maximum for each curve is 1.

$K_{\ell m}$	$\sigma_{\text{Jupiter}}/\sigma_{\text{Earth}}$
γ_0	1.6
K_{22}	2.3
K_{20}	11
$\Re K_{33}$	18
$\Im K_{33}$	18
$\Re K_{32}$	18
$\Im K_{32}$	18
$\Re K_{31}$	25
$\Im K_{31}$	10
K_{30}	53

Table C1. Ratio of posterior uncertainty for all density moments $K_{\ell m}$ between an Earth encounter and a Jupiter encounter with identical properties except for an increased perigee.

The dependence of the exact location of the cadence cut-off is likely more complicated than the above analysis indicates. However, large uncertainties induced by small P_{ω} or large $t_{\text{spin}}/t_{\text{orbit}}$ makes it difficult to produce data which are not affected by the finite size of the prior (as figure 4 is) to study these regimes. Computation time and random variation in σ also limits us. We therefore do not attempt to explore the dependence between T_{cad} and the encounter parameters further. If a future analysis does require a detailed understanding of how cadence affects uncertainty for a specific encounter, our simulation and fit process can be run given the parameters of the encounter in question in a similar manner to section 4.4 to yield more information.

APPENDIX C: COMPARISON OF JUPITER AND EARTH ENCOUNTERS

If sufficiently accurate spin pole data can be detected for non-Earth encounters, it may be possible to extract density moments for encounters with larger planets. In this appendix, we run our reference asteroid through a Jupiter encounter to analyze the differences in uncertainty.

The physical parameters of the asteroid body are kept the same as the Earth encounter case (listed in appendix A), as are the observational uncertainty and cadence. The orbit is adjusted for the Jupiter case by setting a perijove distance of $r_p = 5$ Jupiter radii (compared to perigee radius $r_p = 5$ Earth radii for the Earth encounter). We perform two fits, each with a different value of v_{∞} : in one case we keep the Earth-encounter value of $v_{\infty} = 6 \text{ km s}^{-1}$, and in the other case we increase the velocity such that the eccentricity (and therefore the angle between the orbits' hyperbolic asymptotes) are the same for both encounters. The latter requires $v_{\infty} = \sqrt{G\mu_B/r_p(e-1)} = 32 \text{ km s}^{-1}$. The rationale for these excess velocity values is that, for $v_{\infty} = 6 \text{ km s}^{-1}$, we keep a physically typical encounter excess velocity at the expense of changing the orbit shape, whereas for $v_{\infty} = 32 \text{ km s}^{-1}$ the orbit shape is unchanged, although the asteroid speed is dramatically increased.

Section 4.1 found that v_{∞} does not affect the posterior uncertainties, and indeed we find very little difference between the two v_{∞} cases. We therefore do not distinguish between the two cases further. The ratio between the posterior uncertainties in the Jupiter and the Earth encounters are shown in table C1. In all cases, the Jupiter posteriors are more uncertain than Earth posteriors.

These uncertainty ratios can be understood as follows. The leading order of tidal torque is proportional to μ_A/D^3 . If D/a_B (the ratio of the encounter distance to the central body radius) is roughly constant (as in this case, where $r_p/a_B = 5$), then $\mu_A/D^3 \propto \rho_B$ where ρ_B is the density of the central body. Therefore, little advantage is to be gained by looking for encounters of a massive planet in this sense. Since Jupiter is less dense than Earth, we expect that uncertainty in the first-order parameters γ_0 and K_{2m} would be slightly worse than in the case of Earth, which is seen in table C1.

The second-order terms are damped by an additional factor of a_A/D , which decreases if a massive central body is used. Since Jupiter is about 10 times larger in radius than Earth, we expect that the K_{3m} terms are about ten times more uncertain than the K_{2m} components, which is the case.

The $K_{\ell 0}$ components differ in that $\sigma_{\text{Jupiter}}/\sigma_{\text{Earth}}$ is about five times greater for $K_{\ell 0}$ than other moments of the same ℓ . In fact, K_{30} essentially fills the prior. The special properties of $K_{\ell 0}$ have been analysed noted before, in that they are always more uncertain than other moments and are particularly uncertain in regimes where the asteroid does not tumble after the perigee. In this case, the Jupiter encounter resulted in less tumbling than the Earth encounter, so the larger increase in uncertainty in $K_{\ell 0}$ shown in table C1 is expected.

There are additional effects of central body mass which are not captured in this analysis. For example, encounters with massive planets are more plentiful, so that observation for a fixed period of time will lead to a larger number of observed encounters conducive to low-uncertainty moment extraction (large a_A , small r_p , etc.). The distribution of r_p in this encounter sample will also change; the ratio of the orbit impact parameter (the distance between the orbit asymptotes and the central body) to perigee distance is

$$\frac{b}{r_p} = \sqrt{1 + 2 \frac{G\mu_B}{r_p v_\infty^2}}. \quad (\text{C1})$$

It was mentioned above that the observable perigee distance r_p increases with $a_B \sim \mu_B^{1/3}$, so that $\frac{b}{r_p}$ is larger for more massive planets and therefore the same impact parameter leads to lower periapse. Other effects, such as a change in the physical properties of the encountering asteroids, may also affect the fit uncertainties.

Table C1 shows that an encounter with Jupiter yields less precise posteriors than an encounter with Earth, all else being equal. However, these selection biases will cause more large- a_A and small- r_p asteroids to encounter Jupiter, and therefore yield increased precision. Which of these contradicting effects dominates is not immediately clear, and depends on the specific asteroid population near Jupiter.

APPENDIX D: COMPUTING ASTEROID SHAPE FROM DENSITY MOMENTS

In section 5, we mention that the shape of the asteroid can be computed from observations of the density moments and a_A if a uniform density distribution is assumed. We did not further describe the model in the main text because it is unlike the other three models in the nature of its assumptions, and in the fact that it is non-linear. However, it may be a useful

technique so it is mentioned here; we call it the “surface” model. A similar model was also studied in Ref. [Baxansky & Kiryati \(2007\)](#).

Suppose our asteroid has constant density ρ_0 and known parameters $K_{\ell m}$ and a_A^2 , and that the asteroid is “star shaped” in that every ray originating from the centre of mass of the asteroid (the origin of the body-fixed frame) passes through the surface of the asteroid exactly once, at distance $r(\theta, \phi)$ written in spherical coordinates. By the divergence theorem, we write

$$K_{\ell m} = \frac{\rho_0}{\mu_A a_A^\ell} \oint_{\partial A} d^2 \mathbf{r} \cdot \mathbf{v}(\mathbf{r}) \quad (\text{D1})$$

where $\mathbf{v}(\mathbf{r}) = \hat{\mathbf{r}} R_{\ell m}(\mathbf{r}) r / (3 + \ell)$ so that $\nabla \cdot \mathbf{v}(\mathbf{r}) = R_{\ell m}(\mathbf{r})$. The integral is carried out over the surface of the asteroid. We know the area element satisfies $d^2 \mathbf{r} = (\partial \mathbf{r} / \partial \theta \times \partial \mathbf{r} / \partial \phi) d\theta d\phi$ in our coordinates, and when dotted with $\mathbf{v} \parallel \hat{\mathbf{r}}$, this gives

$$K_{\ell m} = \frac{\rho_0}{\mu_A a_A^\ell (3 + \ell)} \int d\Omega r(\theta, \phi)^3 R_{\ell m}(r(\theta, \phi), \theta, \phi). \quad (\text{D2})$$

where the integral is carried out over the unit sphere. Note that the integrand of each $K_{\ell m}$ is proportional to $r(\theta, \phi)^{(3+\ell)}$ times constants and a spherical harmonic.

We write

$$r(\theta, \phi) = \sum_{\ell m} Y_{\ell m}^* C_{\ell m} \quad (\text{D3})$$

without loss of generality. To keep $r(\theta, \phi) \in \mathbb{R}$, we require $C_{\ell m}^* = (-1)^m C_{\ell, -m} (\ell - m)! / (\ell + m)$. With this definition, equation D2 becomes a polynomial of degree $3 + \ell$ in terms of $C_{\ell m}$ and integrals of products of spherical harmonics. These integrals can be pre-computed so that equation D2 can then be numerically solved via standard polynomial solution methods to find $C_{\ell m}$. A similar equation to equation D2 can be written for a_A

$$a_A^2 = \frac{\rho_0}{5\mu_A} \int d\Omega r(\theta, \phi)^5 \quad (\text{D4})$$

which can also be solved via polynomial methods.

Equations D2 and D4 form a set of $n + 1$ constraints, where n is the number of density moments known. That is, $n = (\ell_{\max} + 1)^2 + 1$, where ℓ_{\max} is the maximum degree of $K_{\ell m}$ known. By setting the same maximum degree on $C_{\ell m}$, we also have n variables plus one for ρ_0 . The system is therefore well-determined and will yield finitely many solutions. These solutions can be further refined by removing those that produce $r(\theta, \phi) < 0$ for any θ, ϕ , which is unphysical. We do not attempt to model uncertainty on the shape.

To test the model, this process was run for an asteroid with $K_{1m} = K_{2m'} = 0$, but randomly chosen K_{3m} . The resulting surface is shown in figure D1. The figure shows a near-spherical asteroid, which is expected for $K_{\ell m} = 0$ for $\ell > 0$. However, the additional K_{3m} components clearly induce non-sphericity in the asteroid which is captured by the surface model.

To give an alternate view of the non-sphericities found via this new surface model, figure D1 also displays the density distribution extracted via the likelihood model assuming a spherical asteroid shape, but with the same density moments. (Uncertainty in the moments is not modelled in this figure, to better compare the two.) Where the likelihood model displays low density, the surface model clearly

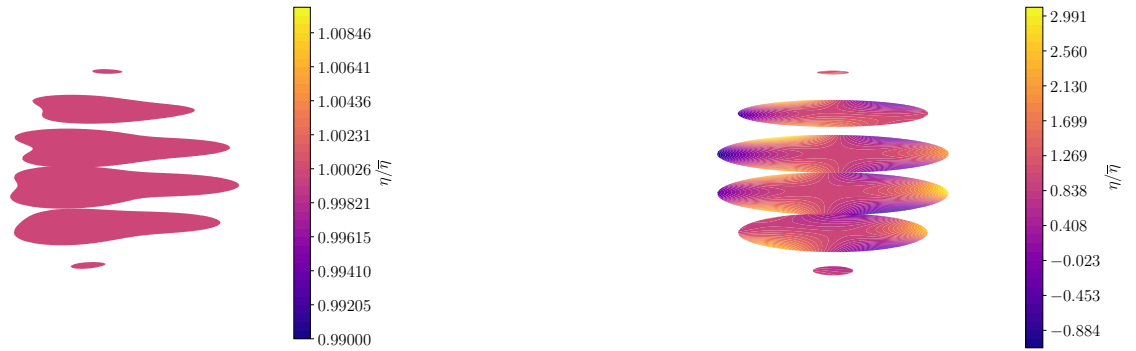


Figure D1. *Left:* the surface of a near-spherical asteroid with uniform density distribution extracted via the surface model. *Right:* the density distribution extracted via the likelihood model for the same density moments but a spherical surface. The same length scale is used in both figures.

retracts into the asteroid. Where the likelihood model yields high density, the surface model extends. Thus, the connection made in section 5.5.2 between non-uniformities in the densities of the likelihood and harmonic models at the asteroid surface and inaccuracies in the surface is more firmly represented.

This surface model could, in principle, be used to improve estimates of the surface of an asteroid made by light curve analysis, since it connects rotational data to the asteroid surface which reflects the light we observe. Thus, uncertainties either in the density moments or the asteroid surface (or both), could be reduced. We only suggest this as a possibility, however, since light-curve analysis is beyond the scope of this paper.

APPENDIX E: EXAMPLE FIT RESULTS

Here, we present example results of the MCMC fit described in section 3.1, applied to encounter data of the asymmetric reference asteroid. The fit results were consistent with the true density moments, and produced consistent data.

Figure E1 shows the spin data with the best-fit overlaid in the top pane and the residuals in the bottom pane. Uncertainties are plotted on the residuals corresponding to the square root of the diagonal entries of the covariance matrix (correlations not included).

Figure E2 shows a corner plot of the ten fitted parameters' posterior distributions, marginalized to functions of one or two variables. The true parameters are shown as lines. Note that the true parameters usually lie within 1- or 2σ of the $\Delta K_{\ell m} = 0$, where $\Delta K_{\ell m}$ is the difference between the posterior $K_{\ell m}$ and the true $K_{\ell m}$.

This paper has been typeset from a TeX/LaTeX file prepared by the author.

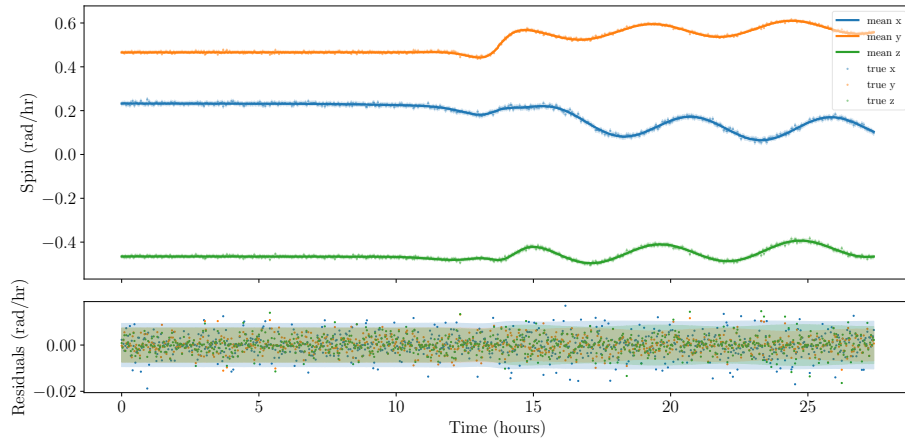


Figure E1. Data, best fit results, and residuals for a fit to synthetic data simulated for an asymmetric reference asteroid. The standard deviation of the data is plotted as an uncertainty band in the residuals plot, but these do not capture covariance between data points.

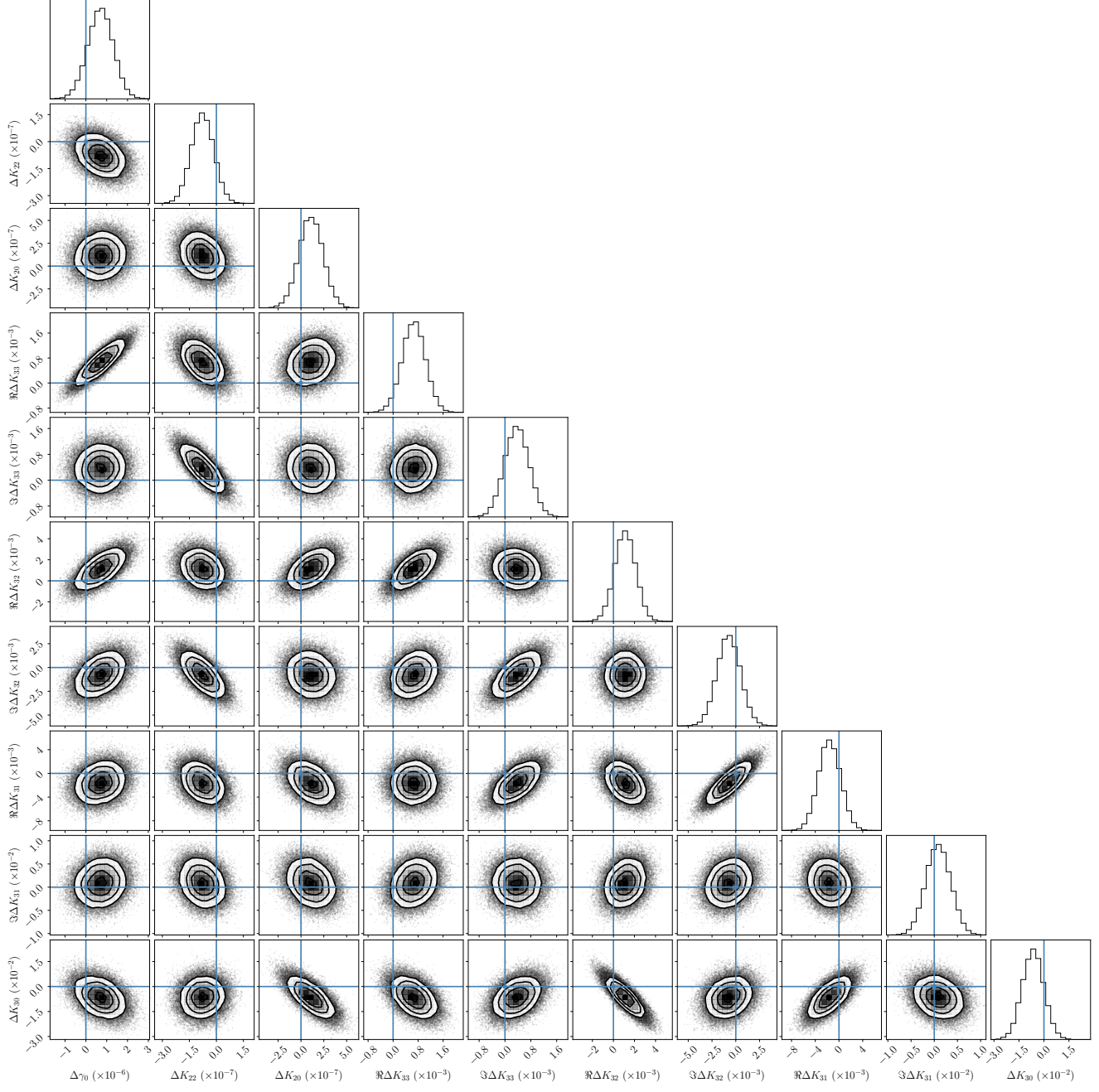


Figure E2. A corner plot for the fit results ten parameters to synthetic data simulated for an asymmetric reference asteroid. Marginal posterior PDFs for each parameter are shown (histograms) along with two-dimensional PDFs (contours). Individual points in the contours are samples from the MCMC fit, and the contours enclose 1-, 2-, and 3- σ of them. True values (which are zero here due to the parameters being displayed relative to the true values) are also shown (blue lines).